THE FAM53C/DYRK1A AXIS REGULATES THE G1/S TRANSITION OF THE CELL CYCLE

Taylar Hammond[1,2], Jong Bin Choi[1], Miles W. Membreño[3], Janos Demeter[4,5], Roy Ng[4,5], Debadrita Bhattacharya[1], Thuyen N. Nguyen[1], Griffin G. Hartmann[1,2], Carine Bossard[6], Jan M. Skotheim[2], Peter K. Jackson[4,5], Anca Pasca[1], Seth M. Rubin[3], and Julien Sage[1,7*]

[1]Departments of Pediatrics, Stanford University, Stanford, CA, USA

[2]Department of Biology, Stanford University, Stanford, CA, USA

[3]Department of Chemistry and Biochemistry, University of California Santa Cruz, Santa Cruz, CA, USA

[4]Department of Microbiology and Immunology, Stanford University, Stanford, CA, USA

[5]Department of Pathology, Stanford University, Stanford, CA, USA

[6]Biosplice Therapeutics Inc., San Diego, CA, USA

[7]Department of Genetics, Stanford University, Stanford, CA, USA

*Correspondence: julsage@stanford.edu

Authors contributions: T.H. performed and analyzed most of the experiments under the supervision of J.S., with guidance from J.M.S.; T.N.N. helped with the mouse colony; D.B. helped with the RNA-seq analysis; J.C. performed the experiments with human organoids under the supervision of A.P.; S.M.R and M.W.M. performed and analyzed the *in vitro* kinase and binding assays; R.N. and J.D. helped with the AP/MS experiments under the supervision of P.K.J.; C.B. provided the DYRK1A inhibitor and guidance on how to use it; T.H. and J.S. wrote the manuscript and prepared the figures together with contributions from all the other authors.

ABSTRACT

A growing number of therapies are being developed to target the cell cycle machinery for the treatment of cancer and other human diseases. Consequently, a greater understanding of the factors regulating cell cycle progression becomes essential to help enhance the response to these new therapies. Here, using data from the Cancer Dependency Map, we identified the poorly-studied factor FAM53C as a new regulator of cell cycle progression. We found that FAM53C is critical for this cell cycle transition and that it acts upstream of the CyclinD-CDK4/6-RB axis in the regulation of the G1/S transition. By mass spectrometry, biochemical, and cellular assays, we identified and validated DYRK1A as a cell cycle kinase that is inhibited by and directly interacts with FAM53C. DYRK1A kinase inhibition rescues the G1 arrest induced by FAM53C knock-down. Consistent with the role for FAM53C identified in cells in culture, *FAM53C* knockout human cortical organoids display increased cell cycle arrest and growth defects. In addition, *Fam53C* knockout mice show defects in body growth and behavioral phenotypes. Because DYRK1A dysregulation contributes to developmental disorders such as Down syndrome as well as tumorigenesis, future strategies aiming at regulating FAM53C activity may benefit a broad range of patients.

INTRODUCTION

The cell cycle is precisely regulated by a complex network of checkpoints. Among those, the G1 checkpoint is an essential decision point for cell cycle progression into S-phase or cell cycle exit in G0, either for a transient arrest, such as quiescence, or for a more permanent arrest, such as during cellular differentiation or senescence. Signal integration at this cell cycle checkpoint is tightly regulated, and defects at this transition can have catastrophic impacts in development and human diseases, including auto-immune diseases and cancer [1]. A better understanding of the mechanisms regulating the G1/S decision point is critical for our understanding of embryonic development, tissue repair and regeneration, and aging processes.

The G1/S transition is regulated by multiple intracellular and extracellular signals, many of which converge onto the RB pathway [2]. The core RB pathway is centered around the retinoblastoma (RB) tumor suppressor. RB normally inhibits cell cycle progression in G1 by interacting with various proteins, including the E2F family of transcription factors, which regulate the expression of genes essential for DNA replication and other aspects of cell division [3]. Under the prevailing model, mitogen signaling stimulates RB hyperphosphorylation and inactivation by Cyclin/CDKs (namely Cyclin D-CDK4/6 and Cyclin E-CDK2), leading to E2F release to promote proliferation; mechanism such as upregulation of the p21 cell cycle inhibitor (p21WAF1/CIP1, encoded by the *CDKN1A* gene) under stress conditions can limit CDK activity to keep cells in G1 arrest [4].

Cyclin D (with three family members Cyclin D1, D2, and D3), is a critical Cyclin whose levels are tightly regulated both at the transcriptional level and the post-transcriptional level, including by regulation of protein stability to induce rapid degradation [5, 6]. Recently, we and others have shown that AMBRA1 (Activating Molecule in Beclin1-Regulated Autophagy) is an adaptor for the CRL4 (CUL4-RING) E3 ubiquitin ligase to mediate the polyubiquitylation and subsequent degradation of cyclin D proteins in cells [7-9]. These studies resolved a long-standing question in

61 the field related to the molecular mechanisms regulating Cyclin protein levels regulation, but also
62 highlighted that, despite decades of research, key regulators of core cell cycle machinery remain
63 to be discovered and characterized.

64 Accumulating evidence also indicates that Dual-specificity Tyrosine Phosphorylation-
65 regulated Kinase 1A (DYRK1A), and its family member DYRK1B, can phosphorylate Cyclin D (at
66 threonine 286, T286, for Cyclin D1), which leads to lower Cyclin D protein levels in cells [10-16]
67 while also modulating p21 levels in a bistable manner [10]. DYRK1A has gained clinical interest
68 due to its dosage sensitive role in cancer and developmental disease: the *DYRK1A* gene maps
69 to the Down syndrome critical region on chromosome 21q22 [17, 18] and increased DYRK1A
70 kinase activity has been linked to many of the developmental brain defects associated with Down
71 syndrome [19-21]. In addition, functional loss of one *DYRK1A* allele leads to the so-called
72 DYRK1A haploinsufficiency syndrome [22]. *DYRK1A* variants have also recently been associated
73 with epilepsy [23]. The regulation of DYRK1A and its effects toward Cyclin D1 and p21 in normal
74 and disease contexts remain poorly understood.

75 Here we aimed to identify new regulators of the G1/S transition of the cell cycle. Using co-
76 dependency data in hundreds of human cancer cell lines from the Cancer Dependency Map
77 Project (DepMap, [24]), we identified the poorly studied protein FAM53C as a candidate cell cycle
78 regulator connected to the RB pathway. Our work shows that FAM53C normally promotes G1/S
79 progression and links its cell cycle activity to DYRK1A activity in cells.

MAIN TEXT

A DepMap analysis identifies FAM53C as a candidate regulator of G1/S.

To identify new candidate regulators of the G1/S switch, we took advantage of the co-dependency scores offered by the Cancer Dependency Map (DepMap) platform to identify potential novel pathway interactors [25, 26]. To find novel interactions, we first generated a list of 38 factors playing a known role at this cell cycle transition (**Supplementary Table S1**). We next overlapped the top 100 co-dependencies from the Cancer Dependency Map (DepMap) platform [27] for each of the input genes to generate a list of shared co-dependency genes from across the input list (**Figure 1A** and **Supplementary Table S2**). We established a score for each gene hit based on the number of input genes which shared a co-dependency with the hit. As expected, high co-dependencies were found between core genes in the RB pathway (e.g., *RB1*, *CCND1*, *AMBRA1*, *CDK4*) (**Figure 1B**), confirming this metric can indicate genuine pathway relationships. The gene coding for CDK2 had the maximum of 13 hits in the analysis, while genes coding for other established G1/S factors such as E2F1 or Cyclin E2 had a score of 3, establishing a cutoff for new candidates; this cutoff score encompassed approximately the top 5% of output values (**Figure 1C** and **Supplementary Table S2**). Among the genes with a score greater or equal to 3 and with no obvious prior direct link to G1 and the RB pathway, we noted *ZZZ3* (score of 6, whose product is a subunit of the Ada-two-A-containing, or ATAC histone acetyltransferase complex [28]) and C1ORF109 (score of 5, whose product is involved in replication stress [29]) (**Supplementary Table S2**). We did not pursue these genes but focused on *FAM53C* (score of 3, Family with sequence similarity 53 C, previously also known as *C5ORF6*) because a similar analysis of DepMap data using a different computational approach also identified this gene as a candidate G1/S regulator [30], and because little is known about FAM53C function.

FAM53C promotes the G1/S transition of the cell cycle.

104 *FAM53C* has a positive co-dependency correlation with *CCND1* and negative correlations with
105 *RB1* and *AMBRA1* (**Figure 1B**), suggesting that FAM53C may normally act as a promoter of cell
106 cycle progression in G1. Indeed, when we acutely knocked-down FAM53C in immortalized human
107 RPE-1 cells using short interfering RNAs (siRNAs) (**Figure 1D**), we observed a significant
108 accumulation of cells in G1/S and loss of S-phase representation in BrdU/PI assays (**Figure 1E**
109 and **Supplementary Figure S1A**). This growth defect was sustained, with no population
110 doublings over 7 days post-transfection (**Figure 1F**). No apoptosis was identified by Annexin V/PI
111 FACS staining, confirming that loss of replication is due to true cell cycle arrest and not cell death
112 (**Supplementary Figure S1B,C**). Conversely, upon FAM53C overexpression (**Figure 1G**), we
113 observed a greater fraction of cells in S-phase and increased number of cells at confluency
114 (**Figure 1H,I** and **Supplementary Figure S1D**). Thus, FAM53C positively regulates the G1/S
115 transition in RPE-1 cells.

116 **The control of G1/S progression by FAM53C is dependent on RB.**

117 FAM53C is conserved throughout vertebrates, but little is known about the function of the
118 FAM53 protein family. Previous work on FAM53B in medaka fish had shown a role in linking DNA-
119 binding proteins to modulators of transcription in the control of proliferation [31]. Previous work on
120 mammalian FAM53A had also suggested a connection with Bone Morphogenetic
121 Protein/Transforming Growth Factor beta (BMP/TGFβ) signaling [32] and with p53 signaling [33].
122 Based on these previous observations suggestive of a link with transcriptional regulation, we
123 performed an RNA sequencing (RNA-seq) analysis of RPE-1 cells with FAM53C knock-down
124 compared to controls. We chose a time point (20 hours after siRNA transfection) before the cell
125 cycle arrest observed upon FAM53C knock-down (~48 hours) to identify possible mechanisms
126 directly downstream of FAM53C rather than mere consequences of the cell cycle arrest. This
127 analysis showed a greater number of genes with downregulated expression compared to
128 upregulated expression (**Supplementary Table S3** and **Supplementary Figure S2A**), but did not

129 readily identify specific gene programs that could directly link FAM53C loss to G1 arrest
130 (**Supplementary Figure S2B,C**).

131 Upon FAM53C knock-down, we found increased mRNA and protein levels for the cell cycle
132 regulator $p21^{CDKN1A}$, which was suggestive of a possible increase in p53 activity (**Figure 2A,B**,
133 **Supplementary Table S3**, and **Supplementary Figure S2D**). However, there were no general
134 changes in the mRNA levels of other canonical p53 target genes [34] (**Supplementary**
135 **Figure S2D**). Moreover, FAM53C knock-down in p53 knockout RPE-1 cells, although it led to
136 lower baseline levels of $p21^{CDKN1A}$, did not rescue the G1 arrest observed upon loss of p53
137 (**Figure 2C** and **Supplementary Figure S2E,F**). Taken together, these results indicate that the
138 control of the G1/S transition by FAM53C in RPE-1 cells is largely p53-independent, and p21
139 upregulation alone cannot explain the G1 arrest in FAM53C-deficient cells.

140 In the original DepMap co-dependency analysis *RB1, CCND1, and CKD4* were key genes
141 contributing to FAM53C's overlap score. Taking this into account, we decided to investigate the
142 pathway interplay between these genes and FAM53C. We found that knockout of RB in RPE-1
143 cells significantly abrogated the G1 arrest observed upon FAM53C knock-down; loss of RB also
144 abrogated the effects of the CDK4/6 inhibitor palbociclib in these experiments, as expected
145 (**Figure 2D** and **Supplementary Figure S2G**). The increased proliferation of RPE-1 cells
146 overexpressing FAM53C could be effectively blocked by palbociclib treatment (**Figure 2E** and
147 **Supplementary Figure S2H**), further suggesting that FAM53C acts upstream of the Cyclin D-
148 CDK4/6-RB module in cell cycle control (**Figure 2F**).

149 **The FAM53C interactome highlights the cell cycle regulatory role of FAM53C.**

150 FAM53C remains a largely uncharacterized protein with no known functional domains [35]. To
151 gain further insights into the mechanisms of action of FAM53C in cells and how FAM53C may
152 connect with the RB pathway, we analyzed the FAM53C interactome in cells. To this end, we
153 expressed a GFP- and S-tagged (localization and affinity purification tag, LAP-tag) lentiviral

154 FAM53C construct in 293T cells, pulled down the FAM53C protein, and performed mass
155 spectrometry on the purified fraction (**Figure 3A** and **Supplementary Figure S3A**). This dual-
156 affinity purification/mass spectroscopy (AP-MS) analysis revealed candidate interactors
157 (**Supplementary Table S4**), with an enrichment for cell cycle factors (**Supplementary Table S5**).
158 Candidate FAM53C interactors in the cell cycle were related to both the G1/S (e.g., CDK4) and
159 the G2/M (e.g., PLK1) transitions, including binding to several subunit of protein phosphatase 2A
160 (PP2A) and several members of the 14-3-3 family, which may contribute to regulation at multiple
161 cell cycle transitions [36, 37] (**Figure 3B** and **Supplementary Table S4**). This analysis further
162 points to a role for FAM53C at the G1/S transition of the cell cycle, but also suggests that FAM53C
163 could play some yet unidentified roles at other phases of the cell cycle.

164 While a specific analysis of the FAM53C interactome has not been performed previously,
165 FAM53C was identified in other pull-down experiments. Integrating our AP/MS data with
166 interactome data from public databases confirmed a likely role for FAM53C in the regulation of
167 cell cycle progression, including the G1/S transition (**Figure 3C**).

168 From these analyses and the DepMap data, DYRK1A stood out as a promising candidate for
169 functional linkage between FAM53C and the control of the G1/S transition. First, previous
170 proteomic studies focusing on the DYRK1A interactome had identified FAM53C in the list of
171 potential partners of DYRK1A [38-41]. Second, our proteomic analysis also identified DCAF7,
172 which is a known functional partner of DYRK1A [42, 43]. Third, a recent study indicates a
173 functional relationship between FAM53C and DYRK1A in neurons [44]. Fourth, strong evidence
174 indicates that DYRK1A kinase activity is a key regulator of the G1/S transition: DYRK1A
175 phosphorylation of LIN52 can promote the activity of the Dimerization Partner, RB-like, E2F, and
176 multivulva class B (DREAM) complex, thereby promoting quiescence [45]; DYRK1A
177 phosphorylation of Cyclin D1 at T286 also results in Cyclin D1 degradation, thereby slowing or
178 preventing G1/S progression [10, 12-14, 46, 47]. To further assess a potential binding interaction

179 between FAM53C and DYRK1A, we used biolayer interferometry (BLI), an optical biosensing
180 technology that quantifies molecular interactions. After affinity purification of FAM53C and
181 DYRK1A expressed from bacteria, a sortase reaction was used to label the N-terminus of
182 DYRK1A with a biotin tag, which allowed us to efficiently load DYRK1A onto streptavidin-coated
183 BLI sensors. FAM53C association to the sensors was then measured in a dose-dependent
184 manner, and rate and binding constants were determined (**Figure 3D**). Using this approach, we
185 found that FAM53C has an affinity for DYRK1A of K_d = 3.3 ± 0.5 μM, confirming the ability of
186 these two proteins to directly interact.

187 Based on these data, while FAM53C likely has several partners in cells, we sought to
188 investigate further the relationship between FAM53C and DYRK1A in G1/S control.

189 **FAM53C acts as an inhibitor of DYRK1A in cells.**

190 Based on the direct binding of FAM53C to DYRK1A and the co-dependency scores between
191 FAM53C, DYRK1A, and Cyclin D1 in the DepMap analysis, we hypothesized that FAM53C may
192 act as a direct inhibitor of DYRK1A kinase activity, in addition to its recently reported role as a
193 regulator of DYRK1A localization in neurons [44]. To this end, we developed a radio-labeling
194 kinase assay utilizing recombinantly expressed DYRK1A, Cyclin D1, and FAM53C. Cyclin D1
195 phosphorylation by DYRK1A has been readily observed *in vitro* at short time points (<30 min) [10,
196 12-14, 46, 47], making it a biochemically and biologically relevant substrate to test FAM53C
197 effects on DYRK1A. Upon titrating increasing amounts of FAM53C, we observed a reduction in
198 Cyclin D1 phosphorylation in this assay (**Figure 4A**). We also noted efficient phosphorylation of
199 FAM53C itself in the presence of DYRK1A (**Figure 4A**), with lower levels of phosphorylation at
200 lower levels of FAM53C, potentially suggestive of a competitive interaction between the two
201 DYRK1A substrates. Phosphorylation of LIN52, another substrate of DYRK1A [45] was also
202 reduced with increasing levels of FAM53C (**Supplementary Figure S4A**). Taken together these
203 data support a model in which FAM53C is a direct inhibitor of DYRK1A kinase activity. Similar

204 observations were made in cells, where we found that the ratio between phosphorylated Cyclin
205 D1 and total Cyclin D1 levels decreased when FAM53C was overexpressed in RPE-1 cells
206 compared to controls (**Figure 4B,C**). This result is expected if FAM53C serves as an inhibitor of
207 DYRK1A. In the context of FAM53C overexpression, DYRK1A inhibition using a highly selective
208 ATP-competitive DYRK1A inhibitor (SM13797 [48]) did not further affect the ratio between
209 phosphorylated Cyclin D1 and total Cyclin D1 levels (**Figure 4B,C**). Conversely, knock-down of
210 FAM53C led to an increase in this ratio (**Supplementary Figure S4B,C**). Thus, *in vitro* and in
211 cells, FAM53C inhibits DYRK1A activity.

212 Based on these observations, we next wondered whether DYRK1A inhibition would rescue
213 the G1 arrest observed upon FAM53C knock-down. We found that this was not the case in wild-
214 type RPE-1 cells (**Figure 4D** and **Supplementary Figure S4D**). However, as noted above, p21
215 levels are increased upon FAM53C knock-down, and this increase in p21 levels was still present
216 despite inhibition of DYRK1A kinase activity (**Figure 4E,F**). This raised the possibility that high
217 levels of p21 were sufficient but not necessary to enforce the G1 arrest observed in this context.
218 Thus, we performed a similar experiment in p53 mutant RPE-1 cells, in which baseline p21 levels
219 are low (**Supplementary Figure S2E**). Indeed, in these p53 deficient RPE-1 cells, inhibition of
220 DYRK1A rescued the G1 arrest observed upon FAM53C knock-down (**Figure 4G** and
221 **Supplementary Figure S4E**). We also found that FAM53C knock-down in p53 wild-type HCT116
222 colon cancer cells led to G1 arrest, which was rescued by treatment with the DYRK1A inhibitor
223 (**Figure 4H** and **Supplementary Figure S4F**). It is notable that HCT116 cells exhibit high
224 dependence on *CCND1* but low dependence on *CDKN1A* in the DepMap dataset as compared
225 to RPE-1-derived cell lines (**Supplementary Figure S4G**), suggesting cell identity may play a
226 role in how cells respond to changes in DYRK1A activity. Overall, these observations indicate that
227 loss of p53 is not always required for the rescue and further support of a model in which DYRK1A
228 activity contributes to the G1 arrest observed upon FAM53C knock-down (**Figure 4I**).

229 **Consequences of *FAM53C* inactivation for embryonic brain development.**

230 Based on the dosage-dependent role of DYRK1A in brain development, we wondered if loss
231 of FAM53C, which can lead to DYRK1A kinase activation, may result in brain developmental
232 phenotypes. As a first way to test this idea, we knocked out *FAM53C* in human induced pluripotent
233 stem cells (iPSCs) using CRISPR/Cas9 (**Figure 5A** and **Supplementary Figure S5A-C**). The
234 *FAM53C* knockout in iPSCs was compatible with their survival and their stemness
235 (**Supplementary Figure S5D,E**), which allowed us to differentiate control and knockout cells into
236 human cortical organoids (hCOs). We noted an increase in the ratio between phosphorylated
237 Cyclin and total Cyclin D1 levels in knockout hCOs compared to controls, together with an
238 increase in p21 levels, similar to the observations in RPE-1 cells (**Figure 5B-D**). Using EdU
239 incorporation assays, we also observed decreased proliferation in the knockout hCOs compared
240 to controls (**Figure 5E** and **Supplementary Figure S5F**), again supporting a role for FAM53C in
241 the promotion of cell cycle progression. Accordingly, FAM53C mutant organoids were smaller in
242 size compared to controls at this stage (**Figure 5F,G**). While a complete analysis of the role of
243 FAM53C in the development of various cell types and structures in hCOs remains to be
244 performed, these observations further support a role for FAM53C in the control of cell cycle
245 progression in G1 in a brain context.

246 ***Fam53C* knockout mice display developmental and behavioral defects.**

247 These data, and developmental roles for DYRK1A also outside of the brain [13, 14, 49] led us
248 to investigate the possible phenotypes of *Fam53C* knockout mice. We obtained mice with a
249 deletion of *Fam53C* exon 4 from the International Mouse Phenotyping Consortium (IPMC) [50]
250 (**Figure 6A**). *Fam53C*$^{-/-}$ and *Fam53C*$^{+/-}$ mice were recovered at the expected frequency from
251 *Fam53C*$^{+/-}$ crosses in the IMPC colony (with a low number of mice analyzed, **Supplementary**
252 **Figure S6A**), but with a significant trend towards fewer of the homozygous mutant mice in our
253 colony at Stanford University (with more mice analyzed, **Figure 6B**). Based on the role of

254 FAM53C in promoting cell cycle progression in G1, *Fam53C*$^{-/-}$ may have been expected to have
255 a reduced body size, similar to Cyclin D1 knockout mice [51, 52]. We observed a significantly
256 lower body mass at weaning for males (**Figure 6C**). This phenotype may be dependent on the
257 husbandry conditions as there was no significant differences in body weight between knockouts
258 and wild-type controls, males or females, in the IMPC dataset (although again with only n=8 mice
259 in each group there) (**Supplementary Figure S6B**). Histological analysis of the brain and other
260 tissues and organs in adult control and knockout mice did not reveal any gross defects
261 (**Supplementary Figure S6C**). Notably, however, the IMPC behavioral analysis showed
262 significant differences between wild-type and *Fam53C*$^{-/-}$ male mice in a "latency to first transition
263 into dark" test, in which the knockout mice showed a decreased exploration of a new environment,
264 suggestive of possibly increased anxiety (n=6 *Fam53C*$^{-/-}$ males and n=7 *Fam53C*$^{-/-}$ females
265 compared to historical controls) (**Figure 6D**). In a survival study, we did not detect any differences
266 between controls and *Fam53C*$^{-/-}$ mice (**Supplementary Figure S6D**). These observations in mice
267 with minimal phenotypes linked to FAM53C loss are in stark contrast to the strong phenotypes
268 observed in cells in culture and suggest mechanisms of compensation *in vivo* that remain to be
269 identified.

DISCUSSION

Here we sought to identify novel regulators of the G1/S transition using the DepMap database. Our analysis led us to focus on FAM53C, a factor which was previously uncharacterized as a cell cycle factor. Our data conclusively place FAM53C upstream of the CycD/CDK4,6-RB pathway at the G1/S transition of the cell cycle. Our data further demonstrate that DYRK1A is a key partner of FAM53C in the control of cell cycle progression at this transition.

DYRK1A controls the G1/S transition of the cell cycle [10, 12, 13, 45-47, 53, 54] but also plays a role in differentiation, especially in developing neurons [21, 55-59]. Thus, it is possible that FAM53C contributes to the control of cellular differentiation, including by regulating the cellular localization of DYRK1A [44], its kinase activity, or by other mechanisms. Because of the role of DYRK1A in the developing brain and in defects associated with Down syndrome [19-21], changes in FAM53C levels and/or activity may be expected to affect brain development. The behavioral data from the International Mouse Phenotyping Consortium (IPMC) support this idea. The cellular basis of this phenotype will require a more in-depth analysis of the brain of mutant mice, possibly at different time points, as our histological analysis did not reveal any major changes in the brain of knockout mice compared to controls in adult animals. Notably, human *FAM53C* variants in public databases are linked to phenotypes such as height and Alzheimer's disease ("co-localization analysis" from the Open Targets Genetics initiative [60]), as well as IGF1 serum levels (data from the Global Biobank Engine [61]). Disruption of IGF1 signaling is a candidate contributor to stunted growth and brain development defects in Down syndrome [62]. These observations provide further rationale to investigate FAM53C function *ex vivo* and *in vivo*, both in the regulation of cell cycle progression and in brain development and function.

Our data indicate that FAM53C controls DYRK1A kinase activity beyond its described ability to control DYRK1A cellular localization [44]. Our phosphorylation assays further suggest that DYRK1A may phosphorylate FAM53C, suggesting a role for FAM53C as a competitive inhibitor

295 against other substrates. But It is also possible that this phosphorylation in turn affects FAM53C
296 localization and/or activity. The identification and the mutation of the DYRK1A phosphorylation
297 site(s) on FAM53C will be a first step to address this point in the future.

298 While our work identifies a FAM53C-DYRK1A-CycD/CDK4,6-RB pathway at the G1/S
299 transition of the cell cycle, it is likely that FAM53C has other functions in cells. In particular, our
300 AP-MS interactome data suggest that FAM53C may play additional roles later in cell cycle,
301 including during G2/M through associations with other kinases like PLK1 and AURKA. Whether
302 these kinase interactions are inhibitory similar to the FAM53C-DYRK1A interaction remains to be
303 determined. We did not observe cell cycle arrest at other stages of the cell cycle beyond G1, but
304 future experiments, including in synchronized cell populations or by single cell tracking, will help
305 address the role of FAM53C at other key checkpoints.

306 With the approval of CDK4/6 inhibitors for the treatment of breast cancer and the development
307 of a variety CDK inhibitors [63-65], it has become even more important than before to better
308 understand the mechanisms regulating the activity of these kinases. Our data indicate that low
309 levels of FAM53C may activate DYRK1A kinase activity towards Cyclin D, thereby decreasing
310 CDK4/6 activity in cells. Our mass spectrometry analysis also identified CDK4 as a possible
311 interactor of FAM53C. Although we did not pursue this observation, a possible direct interaction
312 between FAM53C and CDK4 may also regulate CDK4 activity in cells. This identification of
313 FAM53C as a regulator of the DYRK1A-CycD/CDK4,6-RB pathway suggests that strategies to
314 decrease FAM53C levels in cells may help enhance the anti-tumor effects of CDK inhibitors.

315 **METHODS**

316 **Ethics statement**

317 Mice were maintained at Stanford University's Research Animal Facility according to practices
318 prescribed by the NIH and by the Institutional Animal Care and Use Committee (IACUC) at
319 Stanford University. Additional accreditation of Stanford University Research Animal Facility was
320 provided by the Association for Assessment and Accreditation of Laboratory Animal Care
321 (AAALAC). The study protocol was approved by the Administrative Panel on Laboratory Animal
322 Care (APLAC) at Stanford University (protocol 13565).

323 **Animal studies**

324 We imported *Fam53C* knockout mice from the International Mouse Phenotyping Consortium
325 (IMPC [50], www.mousephenotype.org) (*Fam53*$^{cem1(IMPC)J}$ allele, C57BL/6NJ background). This
326 allele was generated by electroporating the Cas9 protein along with 2 guide sequences 5'-
327 ACTGCATTTTTGAGGAGGAG-3' and 5'-GTTAAAATTCAATACTGCCA-3', which resulted in a
328 1151 bp deletion beginning at Chromosome 18 position 34,767,928 bp and ending after
329 34,769,078 bp (GRCm38/mm10). This mutation deletes exon 4 and 366 bp of flanking intronic
330 sequence including the splice acceptor and donor and is predicted to cause a change of amino
331 acid sequence after residue 46 and early truncation 27 amino acids later. Genotyping was
332 performed using the Mouse Direct PCR kit (for genotyping, B40015) following the protocol
333 provided by the Jackson Laboratory (strain Stock No: 032892, C57BL/6NJ-*Fam53c*$^{em1(IMPC)J/Mmjax}$)
334 using a forward primer for the wild-type allele (5'-CCTGGGAACTCTTCTGTCTAGAGT-3'), a
335 forward primer for the mutant allele (5'-TGGCATTACCACTTCACAGC -3'), and a common
336 reverse primer (5'- CTAAGGACTAACTTGACAGGGCAGA-3') (wild-type band: 99 bp; mutant
337 band: 90 bp).

338 Data generated by the IPMC were downloaded from their web site
339 (https://www.mousephenotype.org/data/genes/MGI:1913556)[50]. For the cohort generated at

340 Stanford to measure body weight and to assess phenotypes during aging, mice were generated
341 from heterozygous crosses.
342 Histological analysis was performed on hematoxylin and eosin-stained paraffin sections prepared
343 by HistoWiz.

344 **DepMap analysis**

345 The DepMap analysis was performed directly from the DepMap portal in 2020 (20q2 datasets)
346 (https://depmap.org/portal)[27].

347 **Cell culture and small molecules**

348 Human cell lines were grown in DMEM high glucose medium supplemented with 10% bovine
349 growth serum (BGS) (Fisher Scientific) and 1% penicillin-streptomycin-glutamine (Gibco). All cell
350 lines tested negative for mycoplasma. RB and p53 mutant RPE-1 cells were a kind gift from
351 Evgeny Zatulovskiy and Jan Skotheim [66]. Control and p53 knockout HCT116 cells were a kind
352 gift from Mengxiong Wang and Laura Attardi.
353 The following small molecule inhibitors were used in cells: palbociclib HCl (Selleckchem #S1116),
354 bortezomib (BTZ, a proteasome inhibitor) (MedChemExpress #HY-10227), and puromycin
355 (ThermoFisher #A1113803). For DYRK1A kinase inhibition, we used SM13797 from Biosplice [48]
356 at a concentration of 1 μM with volume matched DMSO vehicle control unless otherwise noted.
357 Cells were incubated with 500 nM of Bortezomib for 2 hr prior to harvest in experiments evaluating
358 phospho-Cyclin D1 protein level.
359 Human induced pluripotent stem cells (hiPSCs) were cultured in Essential 8 medium (Thermo
360 Fisher Scientific, A1517001) on cell culture plates coated with vitronectin (Thermo Fisher
361 Scientific, 14190). They were passaged approximately every 6 days using 0.5 mM EDTA (Thermo
362 Fisher Scientific, 15575) once they reached about 80% confluency. Cell integrity was confirmed
363 using high-density SNP arrays, and routine PCR testing was performed to ensure cultures
364 remained free of mycoplasma.

365 The differentiation of iPSCs into the three germ layers was performed using the STEMdiff™
366 Trilineage Differentiation Kit (STEMCELL Technologies, #05230).

367 **Knock-down, knock-out, and overexpression**

368 FAM53C knock-down experiments in human cell lines were performed using 5 μM of ON-
369 TARGETplus pooled siRNAs (Horizon – Dharmacon™), and ON-TARGET Control #1 as negative
370 controls. Cells were transfected using the Lipofectamine RNAiMAX reagent, following the
371 manufacturer's recommendations. Lentiviral vectors encoding HA-FAM53C (C-terminal tag)
372 (VectorBuilder) or GFP control (a gift from the Artandi lab). Lentivirus was produced in 293T cells,
373 and cells were infected with viral supernatant on two consecutive days, followed by four days of
374 selection with puromycin.

375 hiPSCs (8×10^5 cells) were electroporated in P3 primary cell nucleofector solution (Lonza, V4XP-
376 3032) with 2 μg of FAM53C KO Plasmid containing GFP expression system (Santa Cruz
377 Biotechnology, sc-412179) using a 4D-Nucleofector (program: DC100) (Lonza). After
378 nucleofection, the cells were transferred to Matrigel-coated plates (Corning, 354277) and cultured
379 in mTESR medium (STEMCELL Technologies, 100-0276) with 10 μM ROCK inhibitor (Y27632)
380 at 37°C for 24 hr. GFP-positive cells were sorted using a FACSAria II flow cytometer (BD
381 Biosciences) and cultured immediately in mTESR medium containing 10 μM Y27632 and Anti-
382 Anti (Thermo Fisher Scientific,15240062). Approximately 300 GFP-positive cells were plated per
383 well in Matrigel-coated six-well plates. Colonies were harvested in QuickExtract DNA Extraction
384 Solution (LGC Biosearch Technologies, QE09050). Then, the genomic region around the
385 CRISPR-Cas9 target site for FAM53C was amplified by PCR using Q5® Hot Start High-Fidelity
386 2X Master Mix (New England Biolabs, M0494S). To select the FAM53C KO clone, we used the
387 following primer pair: forward, 5′-GGCCCAAGATTCCTCTCGAC-3′, and reverse, 5′-
388 GGGTCTCACCCCAGTTTCTC-3′. To examine the specific region of the knockout, RNA was
389 extracted from the initially selected clones using the RNeasy Plus Mini Kit (Qiagen, 74136). cDNA

390 synthesis was then performed using the SuperScript™ IV CellsDirect™ cDNA Synthesis Kit
391 (Invitrogen, 11750150). The cDNA was amplified by PCR and subsequently sequenced. The
392 primers used for this process were: forward, 5′-GCAGACTCTGGATGAGCTGAAATG-3′, and
393 reverse, 5′-TCTCTTGGTGGCAGGGATACT-3′. The sequencing results confirmed that the clone
394 had a deletion of exon 3 and exon 4 (844 bp) (see gene map in Supplementary Figure S5A).
395 Potential off-target effects of the sgRNA were assessed using the RGEN tool
396 (https://www.rgenome.net/), with PCR primers for detecting mutations at potential off-target sites
397 (ZFAND5 (forward, 5′-GCGGCGAGTGCGTTAGT-3′, and reverse, 5′-
398 TTTGTTTCTCTGGGTCGTGGTG-3′), MAP6D1 (forward, 5′-GGCTACTCGGACCTCGACA-3′,
399 and reverse, 5′-GGTTCCAACTCGGCTGAAGG-3′), and DCAF10 (forward, 5′-
400 AAGTTTGGGTCAAGATCCTGGT-3′, and reverse, 5′- AAGGCCAAGTATACTCATAAGTGAGG -
401 3′) (see sequencing results in Supplementary Figure S5B,C).

402 **Generation of hCOs from hiPSCs**

403 The generation of human cortical organoids (hCOs) from hiPSCs followed a previously published
404 protocol [67]. In brief, hiPSCs were dissociated into single cells using Accutase (Innovate Cell
405 Technologies, AT-104) and seeded into AggreWell plates (STEMCELL Technologies, 34815) at a
406 density of 3×10^6 cells per well, using Essential 8 medium (Thermo Fisher Scientific, A1517001)
407 supplemented with 10 μM Rock inhibitor Y-27632 (Selleckchem, S1049). The next day, spheres
408 were collected and transferred to 10 cm ultra-low-attachment dishes (Corning, 3262). For the first
409 6 days, they were cultured in Essential 6 medium (Thermo Fisher Scientific, A1516401) with SB-
410 431542 (10 μM, Tocris, 1614), dorsomorphin (2.5 μM μM Sigma-Aldrich, P5499), and XAV-939
411 (2.5 μM, Tocris, 3748), with daily medium changes. From Day 7, hCOs were maintained to
412 Neurobasal A medium (Thermo Fisher Scientific, 10888) containing B27 (Thermo Fisher
413 Scientific, 12587), along with 20 ng/ml epidermal growth factor (R&D Systems, 236-EG) and 20
414 ng/ml basic fibroblast growth factor (R&D Systems, 233-FB), with daily medium changes for 8

415 days, followed by changes every other day until Day 25. At day 25, the hCOs were switched to a
416 Neurobasal A medium with B27, 20 ng/ml brain-derived neurotrophic factor (BDNF; Peprotech,
417 450-02), and 20 ng/ml NT3 (Peprotech, 450-03) for an additional 20 days, with medium changes
418 every other day. From Day 45 onward, the hCOs were maintained in Neurobasal A medium with
419 B27, with medium changes every 3-4 days.

420 **Quantitative immunoassay, immunoblot analysis, and immunofluorescence**

421 For immunoassays with human cell lines, cells extracts were prepared in RIPA buffer with Roche
422 cOmplete™ ULTRA proteasome and PhosSTOP™ phosphatase inhibitor cocktail tablets
423 (Millipore Sigma #05892791001 and PHOSS-RO). Protein extracts were quantified using the
424 Pierce™ BCA Protein Assay Kit according to manufacturer's instructions (Thermo Fisher
425 Scientific, 23227). For quantitative immunoassays, the capillary-based Simple Western™ assay
426 was performed on the Wes™ system (ProteinSimple) according to the manufacturer's protocol
427 with 1 μg of protein used per lane. Compass software (ProteinSimple) was used for protein
428 quantification, using the default settings unless otherwise specified. For immunoblot analysis, cell
429 lysates were denatured in Laemmli buffer and boiled at 95°C for 5 minutes. 10 μg of protein was
430 loaded into each lane unless otherwise specified. Samples were run on NuPAGE 4 to 12% Bis-
431 Tris gels (Thermo Fisher Scientific # NP0322BOX) and transferred to nitrocellulose membranes
432 using iBlot 2 transfer stacks (Thermo Fisher Scientific IB23002). Membranes were blocked in 10%
433 milk in TBS-T (20 mM Tris, 150 mM NaCl, 0.1% Tween 20) for 1 hr. Primary antibodies were
434 diluted in 5% milk in TBS-T and incubated overnight at 4ºC. Secondary antibodies (Jackson
435 ImmunoResearch anti-rabbit #111-035-144; anti-mouse #115-035-003) were diluted 1:10,000 in
436 5% milk in TBS-T and incubated for 1 hr at room temperature. Chemiluminescence was detected
437 using Amersham ECL Prime Western Blotting Detection Reagent (GE Healthcare #RPN2236).
438 The following primary antibodies were used for human cell lines: HSP90 (1:2000; Cell Signaling
439 Technology, #4877), GAPDH (1:5000; Thermo Fisher, PA5-79289), FAM53C (1:250; Thermo

440 Fisher Scientific, PA5-60125), HA tag (1:1000; Cell Signaling Technology, #3714), p21 (1:1000;
441 Cell Signaling Technology, #2947), Cyclin D1 (1:500; Cell Signaling Technology, #2922), phospho-
442 Cyclin D1 T286 (1:1000; Cell Signaling Technology, #3300), and DYRK1A (1:200; Cell Signaling
443 Technology, #8765).
444 For experiments with hCOs, the organoids were lysed on ice using RIPA buffer with protease and
445 phosphatase inhibitors (Santa Cruz Biotechnology, sc-24948A) through gentle agitation, and
446 incubated at 4ºC for 1 hr. The lysates were then centrifuged at 14,000 × g for 15 minutes, and the
447 supernatant was collected. Protein concentrations in the supernatant were measured using the
448 Pierce™ BCA Protein Assay Kit (Thermo Fisher Scientific, 23225). The lysates were denatured
449 with Bolt™ LDS Sample Buffer (Invitrogen, B0007) at 95°C for 5 minutes. Then, 7 µg of the
450 samples were loaded onto Bolt™ 4-12% Bis-Tris Protein Gels (Invitrogen, NW04120BOX) and
451 transferred to a PVDF membrane using the iBlot™ 2 Transfer Stacks and iBlot2 system (Method:
452 P0) (Thermo Fisher Scientific, IB24002). The membranes were blocked with 5% BSA
453 (GenDEPOT, A0100-005) in TBST (Tris-buffered saline with 0.1% Tween 20, Boston BioProducts,
454 BM-301X) for 1 hr. They were then incubated overnight at 4ºC with primary antibodies in TBST
455 containing 5% BSA: DYRK1A (1:1000; Abcam, ab65220), FAM53C (1:1000; Thermo Fisher
456 Scientific, PIPA5114093), CyclinD1 (1:1000; Cell Signaling, # 2922S), p-CyclinD1 (1:1000; Cell
457 Signaling, #3300), P21 (1:1000; Cell signaling, # 2947S), and β-actin (1:1000; Cell signaling.
458 #4970S). After washing with 5% TBST, the membranes were incubated with horseradish
459 peroxidase-conjugated secondary antibodies at room temperature for 1 hr: Anti-mouse IgG
460 (1:2000; Cell Signaling, #7076), and Anti-rabbit IgG (1:2000; Cell Signaling, #7074). The
461 SuperSignal™ West Femto Maximum Sensitivity Substrate (Thermo Fisher Scientific, 34095) was
462 used for signal development, and the iBright 1500 (Thermo Fisher Scientific, A44114) was used
463 for protein band detection. Band intensities were quantified using ImageJ software (version 1.53t,
464 NIMH, Bethesda, MD) with normalization to background and to the β-actin control.

465 For immunofluorescence analysis of differentiated iPSCs, cells were fixed in a 10% formalin
466 solution (Sigma) at 4ºC for 15 minutes, followed by washing with PBST (PBS with 0.1% Tween
467 20). Permeabilization was carried out using PBS containing 0.1% Triton X-100 (Sigma) for 20
468 minutes. Then, the samples were incubated in 3% BSA for 1 hr before being treated overnight at
469 4ºC with the respective primary antibodies : PAX6 for ectoderm (1:300; BioLegend, PRB-278P),
470 Brachyury for mesoderm (1:300; R&D Systems, AF2085-SP), and SOX17 for endoderm (1:300;
471 Cell Signaling, 81778S). The cells were then rinsed with PBST and incubated with Alexa Fluor-
472 conjugated secondary antibodies (1:500; 488 or 594; Thermo Fisher Scientific) for 1 hr at room
473 temperature. Samples were observed using a Zeiss LSM 980 confocal microscope (Carl Zeiss).

474 **Cell cycle and cell death analyses**

475 Cells were counted using a Countess 3 instrument on default settings (Thermo Fisher Scientific),
476 and dead cells were excluded using 0.4% Trypan Blue solution (Thermo Fisher Scientific,
477 T10282). For palbociclib treatment (with DMSO as a control), cells were treated with 0.5 μM for
478 24 hr. Cell cycle analysis was performed using BrdU pulsed for 2 hr (10 μg/mL, Calbiochem
479 #203806) and propidium iodide (PI) staining[7] unless otherwise indicated. For cell death assays,
480 Annexin V/PI staining was performed and analyzed as described before[7]. Flow cytometry was
481 performed on a BD FACSAria II (BD Biosciences) and data was collected using BD FACSDiva.
482 Data were analyzed using Cytobank Community software (Beckman Coulter Life Sciences).
483 For experiments with hCOs, the EdU assays were performed using the Click-iT™ EdU Alexa
484 Fluor™ 647 Flow Cytometry Assay Kit (Thermo Fisher Scientific, C10424), following the
485 manufacturer's instructions. Briefly, hCOs were incubated with 10 μM EdU for 24 hr, then
486 dissociated using Accutase and resuspended in staining buffer with 3% BSA and 0.5 mM EDTA.
487 After fixation and permeabilization, the cells were incubated with the Click-iT™ reaction cocktail
488 for 30 minutes at room temperature, protected from light. DAPI was added for DNA staining, and

489 the cells were analyzed using a FACSAria II flow cytometer (BD Biosciences) and FCS Express
490 7 software (DeNovo Software).

491 **Bulk RNA sequencing and analysis**

492 For FAM53C knock-down experiments in RPE-1 cells, $1x10^6$ control and siRNA-treated samples
493 were collected in duplicate 20 hours post-transfection, and RNA was isolated using the RNeasy
494 Plus Micro kit (Qiagen #74034). Library preparation and sequencing were performed by
495 Novogene using the Illumina NextSeq 500 platform to obtain ~20 million paired reads/sample.
496 Raw sequencing reads were trimmed using CutAdapt (v2.10)[68] with the TruSeq sequencing
497 adapter (5'-AGATCGGAAGAGCACACGTCTGAACTCCAGTCAC-3'), and a minimum read
498 length of at least 25. Reads were then aligned to the UCSC hg38 genome with HiSat2 [69] using
499 reverse strandedness and discarding unaligned reads. Counts were assigned to genes (hg38
500 GTF) using featureCounts [70] Downstream differential expression analysis was performed using
501 the Deseq2 package [71]. GO term enrichment of differentially expressed genes was performed
502 using ClusterProfiler [72].

503 **FAM53C interactome analysis**

504 Tandem affinity purification

505 10 mL packed cell volume of HEK-293T cells expressing LAP-tagged proteins [73] were re-
506 suspended with 40 mL of LAP-resuspension buffer (300 mM KCl, 50 mM HEPES-KOH [pH 7.4],
507 1 mM EGTA, 1 mM MgCl2, 10% glycerol, 0.5 mM DTT, protease inhibitor [A32965, Thermo Fisher
508 Scientific]), lysed by gradually adding 1200 µL 10% NP-40 to a final concentration of 0.3%, then
509 incubated on ice for 10 min. The lysate was first centrifuged at 14,000 rpm (27,000 g) at 4°C for
510 10 min, and the resulting supernatant was centrifuged at 43,000 rpm (100,000 g) for 1 hr at 4°C
511 to further clarify the lysate. High speed supernatant was mixed with 500 µL of GFP-coupled beads
512 [73] and rotated for 1 hr at 4°C to capture GFP-tagged proteins, then washed five times with 1 mL
513 LAP200N buffer (200 mM KCl, 50 mM HEPES-KOH [pH 7.4], 1 mM EGTA, 1 mM MgCl2, 10%

514 glycerol, protease inhibitors, and 0.05% NP40). After re-suspending the beads with 1 mL
515 LAP200N buffer lacking protease inhibitors, the GFP tag was cleaved by adding 40 µg
516 PreScission-protease and rotating tubes at 4ºC for 16 hr. PreScission-protease eluted
517 supernatant was added to 100 µL of S-protein agarose (69704-3, EMD Millipore) to capture S-
518 tagged protein. After washing three times with LAP200N buffer and twice with LAP0 buffer (50
519 mM HEPES-KOH [pH 7.4], 1 mM EGTA, 1 mM MgCl2, and 10% glycerol), purified protein
520 complexes were eluted with 50 µL of 2X LDS buffer and boiled at 95°C for 3 min. Samples were
521 then run on Bolt Bis-Tris Plus Gels (NW04120BOX, Thermo Fisher Scientific) in Bolt MES SDS
522 Running Buffer (B0002, Thermo Fisher Scientific). Gels were fixed and stained according to
523 Colloidal Blue Staining Kit (LC6025, Thermo Fisher Scientific) with Optima LC/MS grade water
524 (W6-4, Fisher Scientific) at room temperature. The buffer was then replaced with Optima water
525 prior to cutting the bands into eight pieces. The gel slices were then destained, reduced, and
526 alkylated followed by in-gel digestion using (200 ng) Trypsin/LysC (V5073, Promega) as
527 previously [74]. Tryptic peptides were extracted from the gel bands and dried in a speed vac. Prior
528 to LC-MS, each sample was reconstituted in 0.1% formic acid, 2% acetonitrile, and water.

529 Chemicals and Reagents

530 The reagents used in this analysis were obtained from various sources. From Sigma-Aldrich, we
531 obtained 2-Chloroacetamide (CAM; cat. no. C0267), and Potassium hydroxide (KOH; cat. no.
532 P5958). Trifluoroacetic acid (TFA; cat. no. AAL06374AC), Acetic acid (AcOH; cat. no. A11350),
533 Optima™ LC/MS Grade Water (cat. no. W6-4), and 99.5% Formic acid, LC/MS Grade (FA; cat.
534 no. A117-50) were supplied by Fisher Scientific. Tris(2-carboxyethyl)phosphine hydrochloride
535 (TCEP-HCl; cat. no. PG82080) and Halt™ Protease and Phosphatase Inhibitor Cocktails, EDTA-
536 Free (cat. nos. 78425 and 78428, respectively), were purchased from Thermo Fisher Scientific.
537 Honeywell provided the LC/MS grade acetonitrile (ACN; cat. no. 14261-1L). Additionally,
538 Trypsin/Lys-C Mix, Mass Spec Grade (cat. no. V5073) from Promega, and Empore C18 47 mm
539 Extraction Disk (cat. no. 320907D) from Empore were used. Liquid chromatography was

540 conducted using a Bruker PepSep C18 10 cm packed column with 1.5 μm beads and 150 μm I.D
541 (cat. No. 1893483) attached to a ZDV Sprayer with 20 μm I.D (cat. No. 1865710).

542 Stage-Tips Clean Up

543 Homemade Stage-Tips were constructed using two C18 Empore disks, following established
544 procedures. The fabricated Stage-Tips were subjected to a washing process, which involved two
545 washes with 100 μL of methanol, one wash with 100 μL of 80% acetonitrile/0.1% acetic acid, and
546 two washes with 100 μL of 1% acetic acid. Acidified peptides were loaded onto the Stage-Tips.
547 Subsequently, the Stage-Tips were washed three times with 100 μL of 1% acetic acid to remove
548 salts. Finally, the peptides were eluted from the Stage-Tips using two elution steps of 30 μL each,
549 with 60% acetonitrile/0.1% acetic acid as the elution buffer.

550 Liquid Chromatography Setup

551 A nanoELute ultra-high-pressure nano-flow chromatography system was utilized and directly
552 coupled online with a hybrid trapped ion mobility spectrometry—quadrupole time-of-flight mass
553 spectrometer (timsTOF Pro, Bruker) employing a nano-electrospray ion source (CaptiveSpray,
554 Bruker Daltonics).

555 Chromatographic Conditions

556 The liquid chromatography was conducted at a constant temperature of 50°C, employing a
557 reversed-phase column (PepSep column, 10 cm × 150 μm i.d., packed with 1.5 μm C18-coated
558 porous silica beads, Bruker) connected to the 10 μm emitter (Bruker). The mobile phase consisted
559 of two components: Mobile Phase A, comprising water with 0.1/2% formic acid/ACN (v/v), and
560 Mobile Phase B, comprising ACN with 0.1% formic acid (v/v).

561 Gradient Elution

562 Peptide separation was achieved using a linear gradient from 2-33% Mobile Phase B within 60
563 min. This was followed by a washing step with 95% Mobile Phase B and subsequent re-
564 equilibration. The chromatographic process maintained the flow rate at 400 nL/min.

565 MS Acquisition

566 Samples were analyzed using the timsTOF HT Mass Spectrometer in DDA-PASEF mode. The
567 TIMS elution voltage was calibrated linearly to obtain reduced ion mobility coefficients (1/K0) by
568 using three selected ions from the Agilent ESI-L Tuning Mix (m/z 622, 922, 1222). The mass and
569 ion mobility ranges were set from 100 to 1700 m/z and 0.7 to 1.3 1/K0, respectively. Both ramp
570 and acquisition times were set at 100 ms. Precursor ions suitable for PASEF-MS/MS were chosen
571 from TIMS-MS survey scans using the PASEF scheduling algorithm. A polygon filter was applied
572 to the m/z and ion mobility plane to prioritize features likely representing peptide precursors over
573 singly charged background ions. The quadrupole isolation width was set to 2 Th for m/z < 700
574 and 3 Th for m/z > 700, with collision energy linearly increased from 20 to 60 eV as ion mobility
575 ranged from 0.6 to 1.6 (1/K0).

576 Silver staining

577 5 µL of samples containing LDS buffer and DTT prepared for tandem affinity purification and mass
578 spectrometry described above were mixed with 1.25 µL of 500 mM iodoacetamide (0210035105,
579 MP Biomedicals). Proteins were separated in a 4–12% Bis-Tris gel (NP0321BOX, Invitrogen),
580 followed by fixation of the gel overnight in 50% methanol at room temperature. The gel was
581 impregnate with solution C (0.8% (w/v) silver nitrate (S6506, SIGMA), 207.2mM ammonium
582 hydroxide (A6899, SIGMA) and 18.9 mM sodium hydroxide) for 15 min, followed by rinsing with
583 water twice. The image was then developed in solution D (0.005% citric acid and 0.0185%
584 formaldehyde in Milli-Q) until intensity of the bands increase to optimal level. The reaction was
585 then terminated by adding stop solution (45% methanol and 10% acetic acid).

586 Data Analysis

587 Raw mass spec result files were processed using Bionic (Protein Metrics, Inc.) software (version:
588 4.5.2) with the following parameters: precursor mass tolerance: 20 ppm, fragment mass tolerance:
589 40 ppm; fragmentation type: QTOF/HCD; carbamidomethyl as Cys fixed modification, variable
590 modifications of Met oxidation, Asn and Gln deamidation, pyro-Glu formation at N-term Glu and
591 Gln, N-term Acetylation and Ser, Thr and Tyr phosphorylation, with maximum 3 variable

592 modification; trypsin with maximum 2 missed cleavages and fully specific mode; identifications
593 were filtered at 0.01 FDR at the protein level; a fasta library of all human refseq proteins (curated
594 and predicted) was used that was downloaded on 2021/07/20.
595 Spectral counts were normalized to NSAF values [75] and significance of enrichment of bait-
596 association was calculated as described previously [76].

597 **Proteomic analysis**

598 BioGRID [77]. Gene ontology (GO) term enrichment analysis and protein-protein interaction
599 analysis was performed using Metascape with the default settings in the "Express Analysis"
600 function**.** We used Enrichr [78] to analyze the top candidate interactors from the IP/MS
601 experiments (66 proteins, p-val<0.05) on 07/25/2024.

602 **Recombinant protein expression and purification**

603 Recombinant proteins were expressed in *Escherichia coli* BL21 (DE3) cells. The cells were
604 transformed with plasmids encoding the target protein fused with either a His-tag (FAM53C) or a
605 GST-tag (DYRK1A). Transformed BL21 cells were cultured in LB medium supplemented with
606 100μg/mL Ampicillin. Protein expression was induced at an OD_{600} of 0.8 using 1 mM IPTG. The
607 cultures were grown overnight at 20°C.
608 The bacterial cells were harvested by centrifugation and resuspended in lysis buffer containing
609 50 mM Tris-HCl pH 8.0, 150 mM NaCl, and 1 mM TCEP. The cells were lysed by cell homogenizer
610 and clarified by centrifugation. For His-tagged proteins, the lysate was applied to a nickel-
611 nitrilotriacetic acid (Ni-NTA) column pre-equilibrated with equilibration buffer (50 mM Tris-HCl pH
612 8.0, 150 mM NaCl, 1mM TCEP, 10 mM imidazole). After incubation for 30 min, resin with bound
613 protein was washed with the same buffer but containing 30 mM imidazole and subsequently
614 bound proteins were eluted with 200 mM imidazole buffer. For GST-tagged proteins, the lysate
615 was applied to a GST-affinity resin pre-equilibrated with equilibration buffer (50 mM Tris-HCl pH

616 8.0, 150 mM NaCl, 1 mM TCEP), and the protein was eluted using the same buffer but containing
617 20 mM reduced glutathione.
618 The His or GST tag was cleaved by incubating the eluted protein with 0.1 mg/mL GST-TEV
619 protease overnight at 4ºC. Following cleavage, the protein mixture was passed through a GST-
620 affinity column to remove GST-TEV and cleaved tag. The tag-free protein was further purified by
621 ion exchange chromatography using a Q Sepharose column. The protein solution was loaded
622 onto the Q column pre-equilibrated with 50 mM Tris-HCl pH 8.0 and 50 mM NaCl. Bound proteins
623 were eluted using a gradient of 50 mM to 1 M NaCl. As a final purification step, the protein was
624 subjected to size exclusion chromatography on a Superdex 75 column equilibrated with buffer
625 containing 50 mM Tris-HCl pH 8.0, 500 mM NaCl, and 1 mM TCEP. Fractions containing the target
626 protein were pooled and concentrated using centrifugal filtration. The purity of the final protein
627 preparation was confirmed by SDS-PAGE and protein stored at -80°C in 10% glycerol.
628 To obtain biotinylated DYRK1A, we used sortase labeling as described [79], utilizing the N-
629 terminal glycine that is left following TEV cleavage. 50 μM DYRK1A was reacted with 500 μM of
630 a synthetic biotin-LPETGG peptide and a final concentration of 20 μM purified His-tagged sortase
631 in a final reaction volume of 500 μL. The reaction was incubated overnight at 4°C. Following the
632 reaction, the DYRK1A was purified again by passing over Ni^{2+}-NTA and Superdex 75 columns
633 and was stored as above. The Cyclin D1 used in the recombinant protein kinase assay is a
634 complex of CDK4-CycD1 purified as previously described [80].

635 **Kinase assays**

636 Protein samples were mixed in a buffer containing 25 mM Tris-HCl pH 8.0, 150 mM NaCl, 20 mM
637 $MgCl_2$, and 1 mM DTT. A mixture of non-radioactive and [γ- P^{32}] ATP (~10 μCi) was added to the
638 assay samples at a final concentration of 200 nM and allowed to react for 15 or 30 min as
639 indicated. The samples were subjected to SDS-PAGE for protein separation. The SDS-PAGE was
640 performed on a 4-20% gradient at 200V for 40 min under denaturing conditions. Following

641 electrophoresis, the gel was dried down completely to capture the signal from the radiolabeled
642 ATP. The radioactive decay was detected by exposing the dried gel to a phosphor screen
643 overnight. The phosphor screen was scanned using a GE Typhoon Trio Imager.

644 **Biolayer Interferometry**

645 BLI experiments were performed using an eight-channel Octet-RED96e (Santorius). Experiments
646 were performed in an assay buffer containing 25 mM Tris pH 8.0, 150 mM NaCl, 1 mM DTT, 2
647 mg/mL BSA, and 0.2% (v/v) Tween. Samples were formatted in a 96-well plate with each well
648 containing 200 µL. For each experiment, we used eight streptavidin biosensor tips (Santorius)
649 that were loaded with the 200 nM biotinylated DYRK1A and dipped into FAM53C analyte at varied
650 concentrations. All experiments were accompanied by reference measurements using unloaded
651 streptavidin tips dipped into the same analyte-containing wells. Experiments in which analyte
652 concentration was varied also contained a zero-analyte reference. Data were processed and fit
653 using Octet software version 7 (Santorius). Before fitting, all datasets were double reference-
654 subtracted, aligned on the *y* axis through their respective baselines, aligned for interstep
655 correction through their respective dissociation steps, and smoothened using Savitzy–Golay
656 filtering. The first 20 s of association and 20 s of dissociation were used with a 1:1 binding model.
657 The association and dissociation rate constants as well as standard errors were averaged across
658 the set of sensorgrams. The equilibrium dissociation constant K_D was obtained from a steady
659 state analysis of all concentrations of analyte fit to the equation Response = (R_{max} * [Analyte])/(K_D
660 + [Analyte]).

661 **Statistical analysis**

662 Statistical significance was assessed using Prism GraphPad software, unless otherwise stated in
663 the methods above. The tests used are noted in the figure legends and accompanying
664 Supplementary Tables. Data are represented as mean ± standard deviation unless otherwise
665 stated. Statistical significance was assessed using Prism GraphPad software, unless otherwise

stated in the methods above. The tests used are noted in the figure legends and accompanying Supplementary Tables. Data are represented as mean ± standard deviation unless otherwise stated.

Data availability

Sequencing data from RNA sequencing are available from the Gene Expression Omnibus (GEO) under accession numbers GSE282945. The mass spectrometry proteomics data have been deposited to the ProteomeXchange Consortium via the PRIDE [81] repository with the dataset identifier PXD055829 and 10.6019/PXD055829. Data related to the IPMC genotyping and phenotyping of *Fam53C* mutant mice is available on the IPMC web site. All other data are available in the article and supplementary materials, or from the corresponding author upon reasonable request.

Acknowledgements

We thank all the members of the Sage lab for their help and support throughout this study. Research reported in this publication was supported by the NIH (J.S., S.M.R., J.M.S., P.K.J. P01CA254867). J.S. is the Elaine and John Chambers Professor in Pediatric Cancer.

Competing Interest Declaration

C.B. is an employee of Biosplice Therapeutics, Inc. The other authors declare no competing interests.

REFERENCES

1. Matthews HK, Bertoli C, de Bruin RAM. Cell cycle control in cancer. Nat Rev Mol Cell Biol. 2022;23(1):74-88. Epub 20210910. doi: 10.1038/s41580-021-00404-3. PubMed PMID: 34508254.

2. Sherr CJ. G1 phase progression: cycling on cue. Cell. 1994;79(4):551-5.

3. Kent LN, Leone G. The broken cycle: E2F dysfunction in cancer. Nat Rev Cancer. 2019;19(6):326-38. doi: 10.1038/s41568-019-0143-7. PubMed PMID: 31053804.

4. Engeland K. Cell cycle regulation: p53-p21-RB signaling. Cell Death Differ. 2022;29(5):946-60. Epub 20220331. doi: 10.1038/s41418-022-00988-z. PubMed PMID: 35361964; PubMed Central PMCID: PMCPMC9090780.

5. Sherr CJ, Sicinski P. The D-type cyclins: a historical perspective. D-type Cyclins and Cancer: Springer; 2018. p. 1-26.

6. Saleban M, Harris EL, Poulter JA. D-Type Cyclins in Development and Disease. Genes (Basel). 2023;14(7). Epub 20230714. doi: 10.3390/genes14071445. PubMed PMID: 37510349; PubMed Central PMCID: PMCPMC10378862.

7. Chaikovsky AC, Li C, Jeng EE, Loebell S, Lee MC, Murray CW, et al. The AMBRA1 E3 ligase adaptor regulates the stability of cyclin D. Nature. 2021;592(7856):794-8. Epub 2021/04/16. doi: 10.1038/s41586-021-03474-7. PubMed PMID: 33854239.

8. Maiani E, Milletti G, Nazio F, Holdgaard SG, Bartkova J, Rizza S, et al. AMBRA1 regulates cyclin D to guard S-phase entry and genomic integrity. Nature. 2021;592(7856):799-803. Epub 20210414. doi: 10.1038/s41586-021-03422-5. PubMed PMID: 33854232; PubMed Central PMCID: PMCPMC8864551.

9. Simoneschi D, Rona G, Zhou N, Jeong YT, Jiang S, Milletti G, et al. CRL4(AMBRA1) is a master regulator of D-type cyclins. Nature. 2021;592(7856):789-93. Epub 20210414. doi: 10.1038/s41586-021-03445-y. PubMed PMID: 33854235; PubMed Central PMCID: PMCPMC8875297.

10. Chen JY, Lin JR, Tsai FC, Meyer T. Dosage of Dyrk1a shifts cells within a p21-cyclin D1 signaling map to control the decision to enter the cell cycle. Mol Cell. 2013;52(1):87-100. Epub 2013/10/15. doi: 10.1016/j.molcel.2013.09.009. PubMed PMID: 24119401; PubMed Central PMCID: PMCPMC4039290.

11. Ashford AL, Oxley D, Kettle J, Hudson K, Guichard S, Cook SJ, et al. A novel DYRK1B inhibitor AZ191 demonstrates that DYRK1B acts independently of GSK3beta to phosphorylate cyclin D1 at Thr(286), not Thr(288). Biochem J. 2014;457(1):43-56. doi: 10.1042/BJ20130461. PubMed PMID: 24134204.

12. Soppa U, Schumacher J, Florencio Ortiz V, Pasqualon T, Tejedor FJ, Becker W. The Down syndrome-related protein kinase DYRK1A phosphorylates p27(Kip1) and Cyclin D1 and induces cell cycle exit and neuronal differentiation. Cell Cycle. 2014;13(13):2084-100. Epub 20140507. doi: 10.4161/cc.29104. PubMed PMID: 24806449; PubMed Central PMCID: PMCPMC4111700.

13. Thompson BJ, Bhansali R, Diebold L, Cook DE, Stolzenburg L, Casagrande AS, et al. DYRK1A controls the transition from proliferation to quiescence during lymphoid development by

destabilizing Cyclin D3. J Exp Med. 2015;212(6):953-70. doi: 10.1084/jem.20150002. PubMed PMID: 26008897; PubMed Central PMCID: PMCPMC4451127.

14. Hille S, Dierck F, Kuhl C, Sosna J, Adam-Klages S, Adam D, et al. Dyrk1a regulates the cardiomyocyte cell cycle via D-cyclin-dependent Rb/E2f-signalling. Cardiovasc Res. 2016;110(3):381-94. doi: 10.1093/cvr/cvw074. PubMed PMID: 27056896.

15. Belanger F, Roussel C, Sawchyn C, St-Hilaire E, Gezzar-Dandashi S, Kimenyi Ishimwe AB, et al. A genome-wide screen reveals that Dyrk1A kinase promotes nucleotide excision repair by preventing aberrant overexpression of cyclin D1 and p21. J Biol Chem. 2023;299(7):104900. Epub 20230609. doi: 10.1016/j.jbc.2023.104900. PubMed PMID: 37301510; PubMed Central PMCID: PMCPMC10339196.

16. Lindberg MF, Deau E, Miege F, Greverie M, Roche D, George N, et al. Chemical, Biochemical, Cellular, and Physiological Characterization of Leucettinib-21, a Down Syndrome and Alzheimer's Disease Drug Candidate. J Med Chem. 2023;66(23):15648-70. Epub 20231205. doi: 10.1021/acs.jmedchem.3c01888. PubMed PMID: 38051674.

17. Rammohan M, Harris E, Bhansali RS, Zhao E, Li LS, Crispino JD. The chromosome 21 kinase DYRK1A: emerging roles in cancer biology and potential as a therapeutic target. Oncogene. 2022;41(14):2003-11. Epub 2022/02/28. doi: 10.1038/s41388-022-02245-6. PubMed PMID: 35220406; PubMed Central PMCID: PMCPMC8977259.

18. Laham AJ, Saber-Ayad M, El-Awady R. DYRK1A: a down syndrome-related dual protein kinase with a versatile role in tumorigenesis. Cell Mol Life Sci. 2021;78(2):603-19. Epub 2020/09/02. doi: 10.1007/s00018-020-03626-4. PubMed PMID: 32870330.

19. de Souza MM, Cenci AR, Teixeira KF, Machado V, Mendes Schuler MCG, Gon AE, et al. DYRK1A Inhibitors and Perspectives for the Treatment of Alzheimer's Disease. Current Medicinal Chemistry. 2023;30(6):669-88.

20. Wegiel J, Gong CX, Hwang YW. The role of DYRK1A in neurodegenerative diseases. FEBS J. 2011;278(2):236-45. Epub 20101213. doi: 10.1111/j.1742-4658.2010.07955.x. PubMed PMID: 21156028; PubMed Central PMCID: PMCPMC3052627.

21. Ryoo SR, Jeong HK, Radnaabazar C, Yoo JJ, Cho HJ, Lee HW, et al. DYRK1A-mediated hyperphosphorylation of Tau. A functional link between Down syndrome and Alzheimer disease. J Biol Chem. 2007;282(48):34850-7. Epub 20070928. doi: 10.1074/jbc.M707358200. PubMed PMID: 17906291.

22. Ji J, Lee H, Argiropoulos B, Dorrani N, Mann J, Martinez-Agosto JA, et al. DYRK1A haploinsufficiency causes a new recognizable syndrome with microcephaly, intellectual disability, speech impairment, and distinct facies. Eur J Hum Genet. 2015;23(11):1473-81. Epub 20150506. doi: 10.1038/ejhg.2015.71. PubMed PMID: 25944381; PubMed Central PMCID: PMCPMC4613469.

23. Bosselmann CM, Leu C, Brunger T, Hoffmann L, Baldassari S, Chipaux M, et al. Analysis of 1386 epileptogenic brain lesions reveals association with DYRK1A and EGFR. Nat Commun. 2024;15(1):10429. Epub 20241130. doi: 10.1038/s41467-024-54911-w. PubMed PMID: 39616148; PubMed Central PMCID: PMCPMC11608322.

24. McFarland JM, Ho ZV, Kugener G, Dempster JM, Montgomery PG, Bryan JG, et al. Improved estimation of cancer dependencies from large-scale RNAi screens using model-based

normalization and data integration. Nat Commun. 2018;9(1):4610. doi: 10.1038/s41467-018-06916-5. PubMed PMID: 30389920; PubMed Central PMCID: PMCPMC6214982.

25. Takemon Y, LeBlanc VG, Song J, Chan SY, Lee SD, Trinh DL, et al. Multi-Omic Analysis of CIC's Functional Networks Reveals Novel Interaction Partners and a Potential Role in Mitotic Fidelity. Cancers (Basel). 2023;15(10). Epub 20230517. doi: 10.3390/cancers15102805. PubMed PMID: 37345142; PubMed Central PMCID: PMCPMC10216487.

26. Doherty LM, Mills CE, Boswell SA, Liu X, Hoyt CT, Gyori B, et al. Integrating multi-omics data reveals function and therapeutic potential of deubiquitinating enzymes. eLife. 2022;11. Epub 20220623. doi: 10.7554/eLife.72879. PubMed PMID: 35737447; PubMed Central PMCID: PMCPMC9225015.

27. Tsherniak A, Vazquez F, Montgomery PG, Weir BA, Kryukov G, Cowley GS, et al. Defining a Cancer Dependency Map. Cell. 2017;170(3):564-76 e16. doi: 10.1016/j.cell.2017.06.010. PubMed PMID: 28753430; PubMed Central PMCID: PMCPMC5667678.

28. Mi W, Zhang Y, Lyu J, Wang X, Tong Q, Peng D, et al. The ZZ-type zinc finger of ZZZ3 modulates the ATAC complex-mediated histone acetylation and gene activation. Nat Commun. 2018;9(1):3759. Epub 20180914. doi: 10.1038/s41467-018-06247-5. PubMed PMID: 30217978; PubMed Central PMCID: PMCPMC6138639.

29. Krishnamoorthy V, Foglizzo M, Dilley RL, Wu A, Datta A, Dutta P, et al. The SPATA5-SPATA5L1 ATPase complex directs replisome proteostasis to ensure genome integrity. Cell. 2024;187(9):2250-68 e31. Epub 20240329. doi: 10.1016/j.cell.2024.03.002. PubMed PMID: 38554706; PubMed Central PMCID: PMCPMC11055677.

30. Wainberg M, Kamber RA, Balsubramani A, Meyers RM, Sinnott-Armstrong N, Hornburg D, et al. A genome-wide atlas of co-essential modules assigns function to uncharacterized genes. Nat Genet. 2021;53(5):638-49. Epub 2021/04/17. doi: 10.1038/s41588-021-00840-z. PubMed PMID: 33859415.

31. Thermes V, Candal E, Alunni A, Serin G, Bourrat F, Joly JS. Medaka simplet (FAM53B) belongs to a family of novel vertebrate genes controlling cell proliferation. Development. 2006;133(10):1881-90. Epub 20060412. doi: 10.1242/dev.02350. PubMed PMID: 16611694.

32. Bergemann AD, Pagano AS, Reidenberg JS, Simon R, Balboni AL, Laitman JT. Skeletal variations in the Fam53A mutant mouse. Wiley Online Library; 2008.

33. Zhang J, Sun M, Hao M, Diao K, Wang J, Li S, et al. FAM53A Affects Breast Cancer Cell Proliferation, Migration, and Invasion in a p53-Dependent Manner. Frontiers in oncology. 2019;9:1244. Epub 20191114. doi: 10.3389/fonc.2019.01244. PubMed PMID: 31799197; PubMed Central PMCID: PMCPMC6874147.

34. Boutelle AM, Attardi LD. p53 and Tumor Suppression: It Takes a Network. Trends Cell Biol. 2021;31(4):298-310. Epub 20210128. doi: 10.1016/j.tcb.2020.12.011. PubMed PMID: 33518400; PubMed Central PMCID: PMCPMC7954925.

35. Lai F, Godley LA, Fernald AA, Orelli BJ, Pamintuan L, Zhao N, et al. cDNA cloning and genomic structure of three genes localized to human chromosome band 5q31 encoding potential nuclear proteins. Genomics. 2000;70(1):123-30. Epub 2000/11/23. doi: 10.1006/geno.2000.6345. PubMed PMID: 11087669.

807 36. Gardino AK, Yaffe MB, editors. 14-3-3 proteins as signaling integration points for cell cycle
808 control and apoptosis. Seminars in cell & developmental biology; 2011: Elsevier.

809 37. Wlodarchak N, Xing Y. PP2A as a master regulator of the cell cycle. Critical reviews in
810 biochemistry and molecular biology. 2016;51(3):162-84.

811 38. Huttlin EL, Bruckner RJ, Navarrete-Perea J, Cannon JR, Baltier K, Gebreab F, et al. Dual
812 proteome-scale networks reveal cell-specific remodeling of the human interactome. Cell.
813 2021;184(11):3022-40 e28. Epub 2021/05/08. doi: 10.1016/j.cell.2021.04.011. PubMed PMID:
814 33961781; PubMed Central PMCID: PMCPMC8165030.

815 39. Menon VR, Ananthapadmanabhan V, Swanson S, Saini S, Sesay F, Yakovlev V, et al.
816 DYRK1A regulates the recruitment of 53BP1 to the sites of DNA damage in part through
817 interaction with RNF169. Cell Cycle. 2019;18(5):531-51. Epub 2019/02/19. doi:
818 10.1080/15384101.2019.1577525. PubMed PMID: 30773093; PubMed Central PMCID:
819 PMCPMC6464593.

820 40. Roewenstrunk J, Di Vona C, Chen J, Borras E, Dong C, Arato K, et al. A comprehensive
821 proteomics-based interaction screen that links DYRK1A to RNF169 and to the DNA damage
822 response. Scientific reports. 2019;9(1):6014. Epub 2019/04/14. doi: 10.1038/s41598-019-42445-
823 x. PubMed PMID: 30979931; PubMed Central PMCID: PMCPMC6461666.

824 41. Guard SE, Poss ZC, Ebmeier CC, Pagratis M, Simpson H, Taatjes DJ, et al. The nuclear
825 interactome of DYRK1A reveals a functional role in DNA damage repair. Scientific reports.
826 2019;9(1):6539. Epub 2019/04/27. doi: 10.1038/s41598-019-42990-5. PubMed PMID: 31024071;
827 PubMed Central PMCID: PMCPMC6483993.

828 42. Glenewinkel F, Cohen MJ, King CR, Kaspar S, Bamberg-Lemper S, Mymryk JS, et al. The
829 adaptor protein DCAF7 mediates the interaction of the adenovirus E1A oncoprotein with the
830 protein kinases DYRK1A and HIPK2. Scientific reports. 2016;6:28241. Epub 20160616. doi:
831 10.1038/srep28241. PubMed PMID: 27307198; PubMed Central PMCID: PMCPMC4910162.

832 43. Xiang J, Yang S, Xin N, Gaertig MA, Reeves RH, Li S, et al. DYRK1A regulates Hap1-
833 Dcaf7/WDR68 binding with implication for delayed growth in Down syndrome. Proc Natl Acad Sci
834 U S A. 2017;114(7):E1224-E33. Epub 20170130. doi: 10.1073/pnas.1614893114. PubMed PMID:
835 28137862; PubMed Central PMCID: PMCPMC5321030.

836 44. Miyata Y, Nishida E. Identification of FAM53C as a cytosolic-anchoring inhibitory binding
837 protein of the kinase DYRK1A. Life Sci Alliance. 2023;6(12). Epub 20231006. doi:
838 10.26508/lsa.202302129. PubMed PMID: 37802655; PubMed Central PMCID:
839 PMCPMC10559228.

840 45. Litovchick L, Florens LA, Swanson SK, Washburn MP, Decaprio JA. DYRK1A protein
841 kinase promotes quiescence and senescence through DREAM complex assembly. Genes Dev.
842 2011;25(8):801-13. Epub 2011/04/19. doi: 25/8/801 [pii]

843 10.1101/gad.2034211. PubMed PMID: 21498570.

844 46. Massey AJ, Benwell K, Burbridge M, Kotschy A, Walmsley DL. Targeting DYRK1A/B
845 kinases to modulate p21-cyclin D1-p27 signalling and induce anti-tumour activity in a model of
846 human glioblastoma. J Cell Mol Med. 2021;25(22):10650-62. Epub 2021/10/29. doi:
847 10.1111/jcmm.17002. PubMed PMID: 34708541; PubMed Central PMCID: PMCPMC8581321.

848 47. Najas S, Arranz J, Lochhead PA, Ashford AL, Oxley D, Delabar JM, et al. DYRK1A-
849 mediated Cyclin D1 Degradation in Neural Stem Cells Contributes to the Neurogenic Cortical
850 Defects in Down Syndrome. EBioMedicine. 2015;2(2):120-34. doi: 10.1016/j.ebiom.2015.01.010.
851 PubMed PMID: 26137553; PubMed Central PMCID: PMCPMC4484814.

852 48. Jarvis MC, Mittapalli G, Creger E, Nora C, Ibanez M, Bhat D, et al. Next-generation
853 DYRK1A inhibitors as a new therapeutic approach for the treatment of hematological
854 malignancies. Cancer Research. 2023;83(7_Supplement):5019-.

855 49. van Bon BWM, Coe BP, de Vries BBA, Eichler EE. DYRK1A Syndrome. In: Adam MP,
856 Mirzaa GM, Pagon RA, Wallace SE, Bean LJH, Gripp KW, et al., editors. GeneReviews((R)).
857 Seattle (WA)1993.

858 50. Groza T, Gomez FL, Mashhadi HH, Munoz-Fuentes V, Gunes O, Wilson R, et al. The
859 International Mouse Phenotyping Consortium: comprehensive knockout phenotyping
860 underpinning the study of human disease. Nucleic Acids Res. 2023;51(D1):D1038-D45. doi:
861 10.1093/nar/gkac972. PubMed PMID: 36305825; PubMed Central PMCID: PMCPMC9825559.

862 51. Sicinski P, Donaher JL, Parker SB, Li T, Fazeli A, Gardner H, et al. Cyclin D1 provides a
863 link between development and oncogenesis in the retina and breast. Cell. 1995;82(4):621-30. doi:
864 10.1016/0092-8674(95)90034-9. PubMed PMID: 7664341.

865 52. Fantl V, Stamp G, Andrews A, Rosewell I, Dickson C. Mice lacking cyclin D1 are small and
866 show defects in eye and mammary gland development. Genes Dev. 1995;9(19):2364-72. doi:
867 10.1101/gad.9.19.2364. PubMed PMID: 7557388.

868 53. Tschop K, Conery AR, Litovchick L, Decaprio JA, Settleman J, Harlow E, et al. A kinase
869 shRNA screen links LATS2 and the pRB tumor suppressor. Genes Dev. 2011;25(8):814-30. Epub
870 2011/04/19. doi: 25/8/814 [pii]

871 10.1101/gad.2000211. PubMed PMID: 21498571.

872 54. Kruitwagen HS, Westendorp B, Viebahn CS, Post K, van Wolferen ME, Oosterhoff LA, et
873 al. DYRK1A Is a Regulator of S-Phase Entry in Hepatic Progenitor Cells. Stem Cells Dev.
874 2018;27(2):133-46. doi: 10.1089/scd.2017.0139. PubMed PMID: 29179659.

875 55. Laguna A, Barallobre MJ, Marchena MA, Mateus C, Ramirez E, Martinez-Cue C, et al.
876 Triplication of DYRK1A causes retinal structural and functional alterations in Down syndrome.
877 Hum Mol Genet. 2013;22(14):2775-84. Epub 20130319. doi: 10.1093/hmg/ddt125. PubMed
878 PMID: 23512985.

879 56. Mejecase C, Way CM, Owen N, Moosajee M. Ocular Phenotype Associated with DYRK1A
880 Variants. Genes (Basel). 2021;12(2). Epub 20210205. doi: 10.3390/genes12020234. PubMed
881 PMID: 33562844; PubMed Central PMCID: PMCPMC7915179.

882 57. Wegiel J, Kuchna I, Nowicki K, Frackowiak J, Dowjat K, Silverman WP, et al. Cell type-
883 and brain structure-specific patterns of distribution of minibrain kinase in human brain. Brain Res.
884 2004;1010(1-2):69-80. Epub 2004/05/06. doi: 10.1016/j.brainres.2004.03.008. PubMed PMID:
885 15126119.

886 58. Gockler N, Jofre G, Papadopoulos C, Soppa U, Tejedor FJ, Becker W. Harmine specifically
887 inhibits protein kinase DYRK1A and interferes with neurite formation. FEBS J.
888 2009;276(21):6324-37. Epub 2009/10/03. doi: 10.1111/j.1742-4658.2009.07346.x. PubMed
889 PMID: 19796173.

59. Neumann F, Gourdain S, Albac C, Dekker AD, Bui LC, Dairou J, et al. DYRK1A inhibition and cognitive rescue in a Down syndrome mouse model are induced by new fluoro-DANDY derivatives. Scientific reports. 2018;8(1):2859. doi: 10.1038/s41598-018-20984-z. PubMed PMID: 29434250; PubMed Central PMCID: PMCPMC5809559.

60. Ghoussaini M, Mountjoy E, Carmona M, Peat G, Schmidt EM, Hercules A, et al. Open Targets Genetics: systematic identification of trait-associated genes using large-scale genetics and functional genomics. Nucleic Acids Res. 2021;49(D1):D1311-D20. doi: 10.1093/nar/gkaa840. PubMed PMID: 33045747; PubMed Central PMCID: PMCPMC7778936.

61. McInnes G, Tanigawa Y, DeBoever C, Lavertu A, Olivieri JE, Aguirre M, et al. Global Biobank Engine: enabling genotype-phenotype browsing for biobank summary statistics. Bioinformatics. 2019;35(14):2495-7. doi: 10.1093/bioinformatics/bty999. PubMed PMID: 30520965; PubMed Central PMCID: PMCPMC6612820.

62. Araya P, Kinning KT, Coughlan C, Smith KP, Granrath RE, Enriquez-Estrada BA, et al. IGF1 deficiency integrates stunted growth and neurodegeneration in Down syndrome. Cell reports. 2022;41(13):111883. doi: 10.1016/j.celrep.2022.111883. PubMed PMID: 36577365; PubMed Central PMCID: PMCPMC9876612.

63. Sherr CJ, Beach D, Shapiro GI. Targeting CDK4 and CDK6: From Discovery to Therapy. Cancer Discov. 2016;6(4):353-67. doi: 10.1158/2159-8290.CD-15-0894. PubMed PMID: 26658964; PubMed Central PMCID: PMCPMC4821753.

64. Suski JM, Braun M, Strmiska V, Sicinski P. Targeting cell-cycle machinery in cancer. Cancer Cell. 2021;39(6):759-78. Epub 2021/04/24. doi: 10.1016/j.ccell.2021.03.010. PubMed PMID: 33891890; PubMed Central PMCID: PMCPMC8206013.

65. Goel S, Bergholz JS, Zhao JJ. Targeting CDK4 and CDK6 in cancer. Nat Rev Cancer. 2022;22(6):356-72. Epub 20220318. doi: 10.1038/s41568-022-00456-3. PubMed PMID: 35304604; PubMed Central PMCID: PMCPMC9149100.

66. Zatulovskiy E, Zhang S, Berenson DF, Topacio BR, Skotheim JM. Cell growth dilutes the cell cycle inhibitor Rb to trigger cell division. Science. 2020;369(6502):466-71. doi: 10.1126/science.aaz6213. PubMed PMID: 32703881; PubMed Central PMCID: PMCPMC7489475.

67. Yoon SJ, Elahi LS, Pasca AM, Marton RM, Gordon A, Revah O, et al. Reliability of human cortical organoid generation. Nat Methods. 2019;16(1):75-8. Epub 20181220. doi: 10.1038/s41592-018-0255-0. PubMed PMID: 30573846; PubMed Central PMCID: PMCPMC6677388.

68. Martin M. Cutadapt removes adapter sequences from high-throughput sequencing reads. EMBnet journal. 2011;17(1):10-2.

69. Kim D, Paggi JM, Park C, Bennett C, Salzberg SL. Graph-based genome alignment and genotyping with HISAT2 and HISAT-genotype. Nat Biotechnol. 2019;37(8):907-15. Epub 2019/08/04. doi: 10.1038/s41587-019-0201-4. PubMed PMID: 31375807; PubMed Central PMCID: PMCPMC7605509.

70. Liao Y, Smyth GK, Shi W. featureCounts: an efficient general purpose program for assigning sequence reads to genomic features. Bioinformatics. 2014;30(7):923-30. Epub 2013/11/15. doi: 10.1093/bioinformatics/btt656. PubMed PMID: 24227677.

932 71. Love MI, Huber W, Anders S. Moderated estimation of fold change and dispersion for
933 RNA-seq data with DESeq2. Genome Biol. 2014;15(12):550. Epub 2014/12/18. doi:
934 10.1186/s13059-014-0550-8. PubMed PMID: 25516281; PubMed Central PMCID:
935 PMCPMC4302049.

936 72. Wu T, Hu E, Xu S, Chen M, Guo P, Dai Z, et al. clusterProfiler 4.0: A universal enrichment
937 tool for interpreting omics data. Innovation (Camb). 2021;2(3):100141. Epub 2021/09/25. doi:
938 10.1016/j.xinn.2021.100141. PubMed PMID: 34557778; PubMed Central PMCID:
939 PMCPMC8454663.

940 73. Torres JZ, Miller JJ, Jackson PK. High-throughput generation of tagged stable cell lines
941 for proteomic analysis. Proteomics. 2009;9(10):2888-91. doi: 10.1002/pmic.200800873. PubMed
942 PMID: 19405035; PubMed Central PMCID: PMCPMC4785821.

943 74. Shevchenko A, Tomas H, Havlis J, Olsen JV, Mann M. In-gel digestion for mass
944 spectrometric characterization of proteins and proteomes. Nat Protoc. 2006;1(6):2856-60. doi:
945 10.1038/nprot.2006.468. PubMed PMID: 17406544.

946 75. Zybailov B, Mosley AL, Sardiu ME, Coleman MK, Florens L, Washburn MP. Statistical
947 analysis of membrane proteome expression changes in Saccharomyces cerevisiae. J Proteome
948 Res. 2006;5(9):2339-47. doi: 10.1021/pr060161n. PubMed PMID: 16944946.

949 76. Ding S, Mooney N, Li B, Kelly MR, Feng N, Loktev AV, et al. Comparative Proteomics
950 Reveals Strain-Specific beta-TrCP Degradation via Rotavirus NSP1 Hijacking a Host Cullin-3-
951 Rbx1 Complex. PLoS Pathog. 2016;12(10):e1005929. doi: 10.1371/journal.ppat.1005929.
952 PubMed PMID: 27706223; PubMed Central PMCID: PMCPMC5051689.

953 77. Oughtred R, Rust J, Chang C, Breitkreutz BJ, Stark C, Willems A, et al. The BioGRID
954 database: A comprehensive biomedical resource of curated protein, genetic, and chemical
955 interactions. Protein Sci. 2021;30(1):187-200. Epub 2020/10/19. doi: 10.1002/pro.3978. PubMed
956 PMID: 33070389; PubMed Central PMCID: PMCPMC7737760.

957 78. Chen EY, Tan CM, Kou Y, Duan Q, Wang Z, Meirelles GV, et al. Enrichr: interactive and
958 collaborative HTML5 gene list enrichment analysis tool. BMC Bioinformatics. 2013;14:128. Epub
959 2013/04/17. doi: 10.1186/1471-2105-14-128. PubMed PMID: 23586463; PubMed Central
960 PMCID: PMC3637064.

961 79. Theile CS, Witte MD, Blom AE, Kundrat L, Ploegh HL, Guimaraes CP. Site-specific N-
962 terminal labeling of proteins using sortase-mediated reactions. Nat Protoc. 2013;8(9):1800-7.
963 Epub 20130829. doi: 10.1038/nprot.2013.102. PubMed PMID: 23989674; PubMed Central
964 PMCID: PMCPMC3941705.

965 80. Guiley KZ, Stevenson JW, Lou K, Barkovich KJ, Kumarasamy V, Wijeratne TU, et al. p27
966 allosterically activates cyclin-dependent kinase 4 and antagonizes palbociclib inhibition. Science.
967 2019;366(6471). doi: 10.1126/science.aaw2106. PubMed PMID: 31831640.

968 81. Vizcaino JA, Csordas A, Del-Toro N, Dianes JA, Griss J, Lavidas I, et al. 2016 update of
969 the PRIDE database and its related tools. Nucleic Acids Res. 2016;44(22):11033. doi:
970 10.1093/nar/gkw880. PubMed PMID: 27683222; PubMed Central PMCID: PMCPMC5159556.

FIGURES

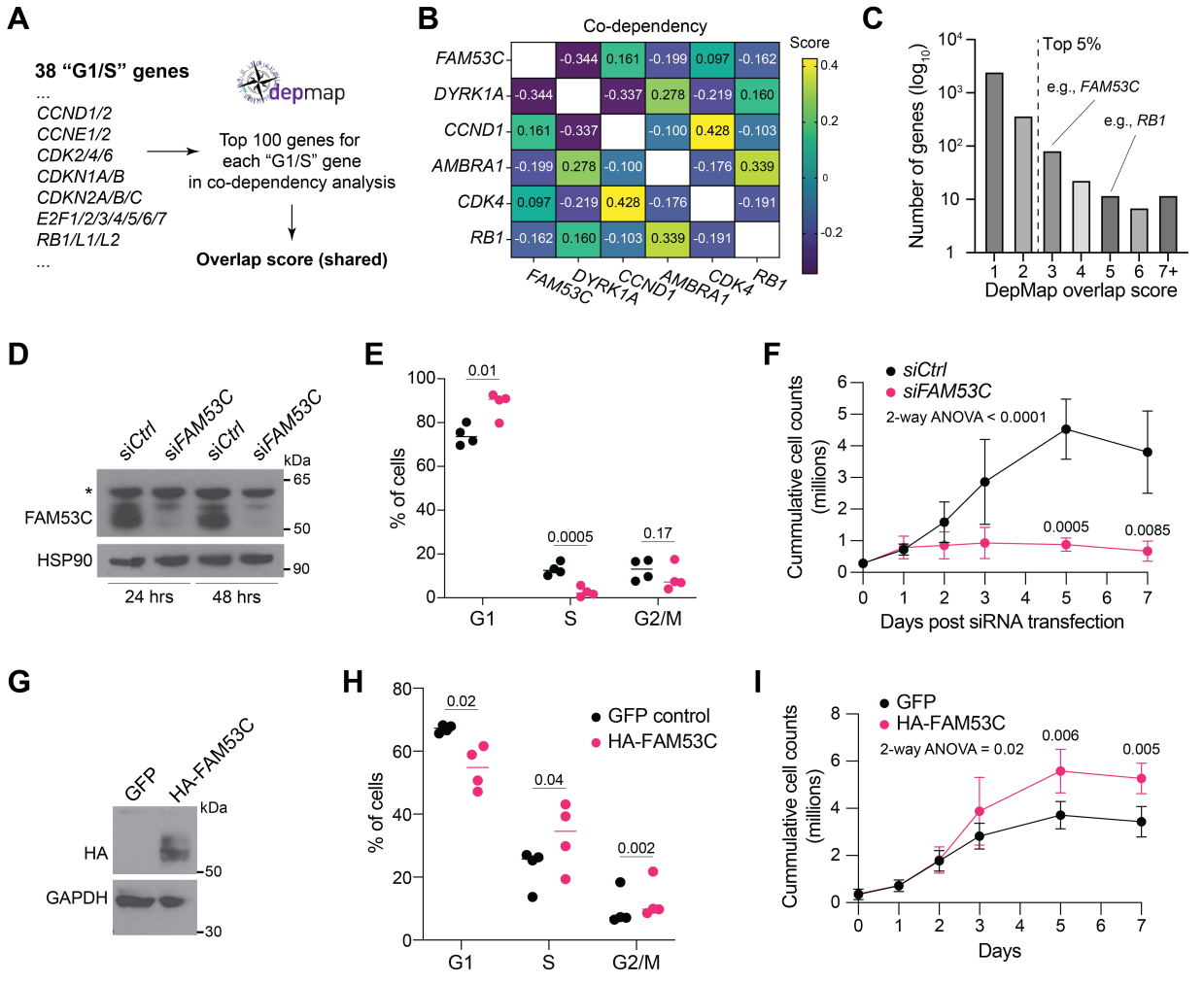

Figure 1: Identification of FAM53C as a positive regulator of cell cycle progression in G1.

A. Strategy to identify new cell cycle regulators using the DepMap database. See Supplementary Table S1 for the complete list of the 38 genes and associated DepMap data.

B. Heatmap of correlation scores from the DepMap analysis with 6 cell cycle genes.

C. Representation of the number of genes with different overlap scores in the DepMap analysis. *RB1* and *FAM53C* are indicated; the maximal overlap score was 13 for the *CDK2* (not shown on graph). The cut-off overlap score value for top candidates was set at 3 (top 5%). See Supplementary Table S2 for complete data.

D. Immunoblot analysis for FAM53C in knock-down (si*FAM53C*) RPE-1 cells compared to controls (si*Ctrl*) at 24 h and 48 h. HSP90 serves as a loading control. Molecular weights are indicated in kDa. *, non-specific signal.

E. Cell cycle analysis by BrdU/PI staining in control and FAM53C knock-down cells (N=4).

F. Population growth analysis (cell counts) in control and FAM53C knock-down cells (N=3-5).

986 **G.** Representative (n=3) immunoblot analysis for FAM53C overexpression (HA-tagged FAM53C)
987 compared to control cells (with GFP expression) in RPE-1 cells. GAPDH serves as a loading
988 control. Molecular weights are indicated in kDa.

989 **H.** Cell cycle analysis by BrdU/PI staining in control and FAM53C-overexpressing cells (n=4).

990 **I.** Population growth analysis in control and FAM53C-overexpressing cells (n=3-5).

991 P-values for (E) and (H) were calculated by paired t-test. P-values for (F) and (I) were calculated
992 by mixed-model ANOVA followed by post-hoc paired two-tail t-test.

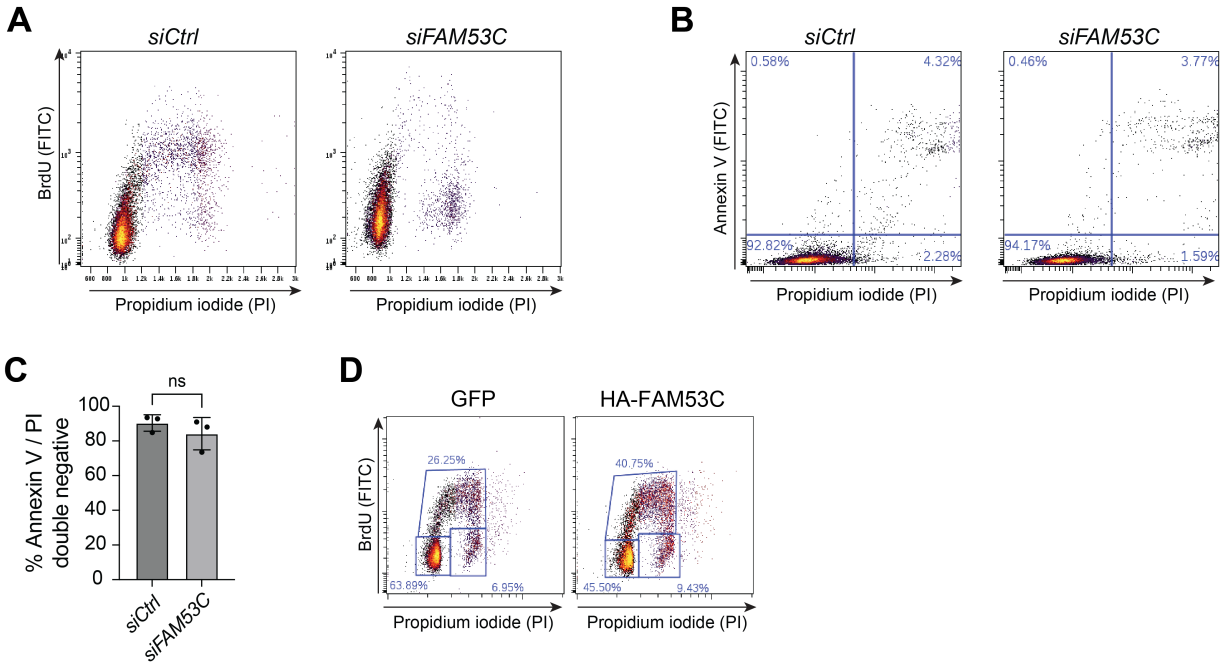

Figure S1 related to Figure 1: Identification of FAM53C as a positive regulator of cell cycle progression in G1.

A. Representative example of flow cytometry analysis for BrdU/PI staining of RPE-1 cells with control siRNAs and FAM53C siRNAs (related to Figure 1E).

B. Representative example of flow cytometry analysis for Annexin V/PI staining of RPE-1 cells with control siRNAs and FAM53C siRNAs. The double negative cells are the live cells.

C. Quantification of (B) (N=3).

D. Representative example of flow cytometry analysis for BrdU/PI staining of RPE-1 cells with GFP or FAM53C overexpression.

P-values for (C) were calculated by t-test.

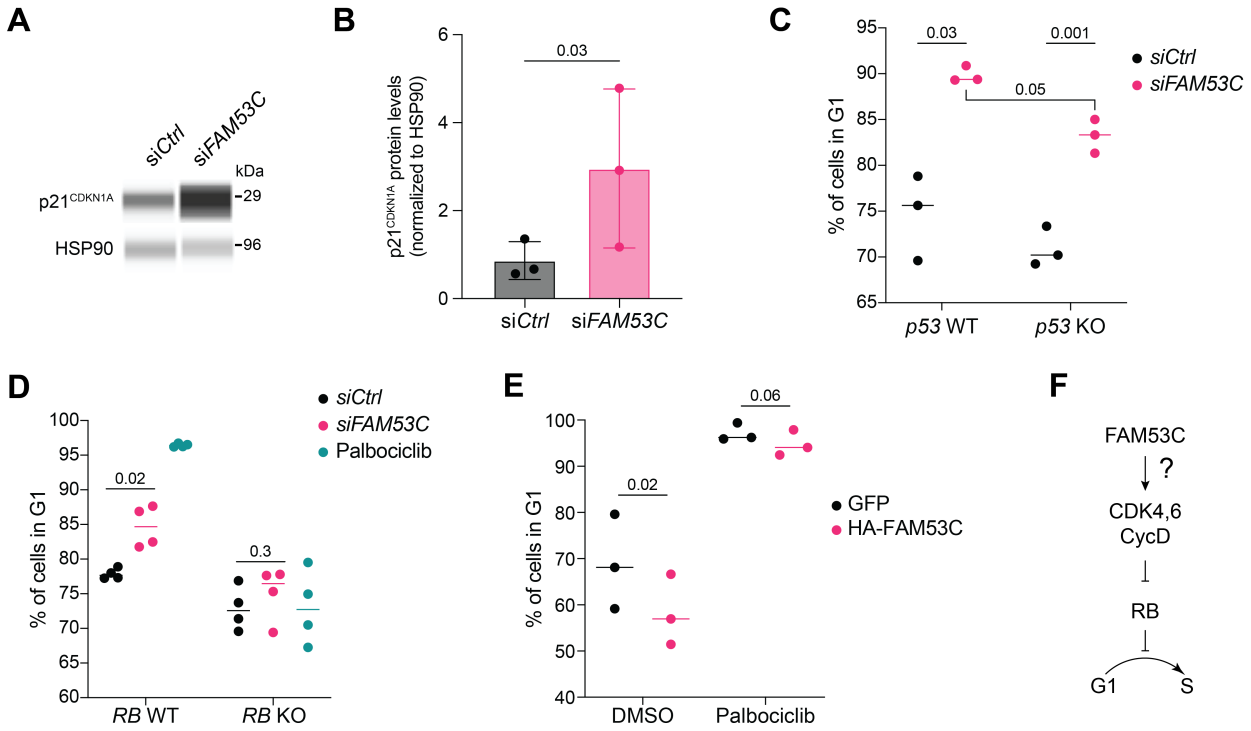

Figure 2: The G1 arrest induced by FAM53C knock-down is dependent on RB.

A. Representative immunoassay for p21 in control (*siCtrl)*and FAM53C knock-down (si*FAM53C*) RPE-1 cells. HSP90 serves as a loading control. Molecular weights are indicated in kDa.

B. Quantification of (A) (N=3).

C. Fraction of cells in G1 from BrdU/PI staining in control (wild-type, WT) and p53 knockout (KO) RPE-1 cells, with or without FAM53C knock-down (N=3).

D. As in (C) control and RB knockout RPE-1 cells (N=4).

E. Fraction of cells in G1 from BrdU/PI staining in control (GFP) and FAM53C-overexpressing RPE-1 cells, with or without palbociclib treatment (N=3).

F. Cartoon placing FAM53C upstream of the CycD/CDK4,6-RB pathway in G1.

P-values for (B) calculated by ratio paired t-test. P-values for (C), (D), (E) calculated by paired t-test.

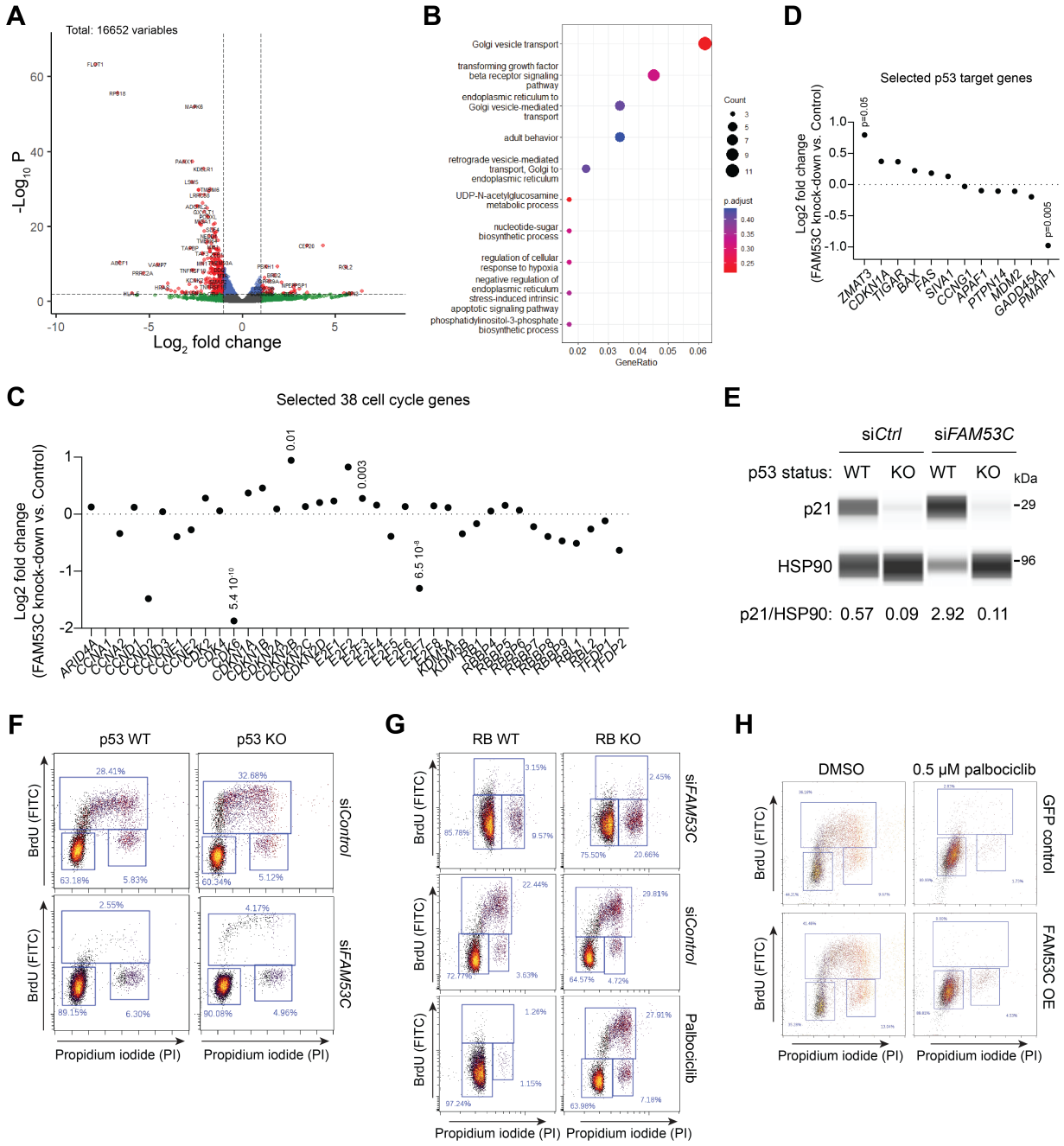

Figure S2, related to Figure 2: The G1 arrest induced by FAM53C knock-down is dependent on RB.

A. Volcano plot from the RNA-seq data comparing control and FAM53C knock-down RPE-1 cells (20 hr after siRNA transfection). See Supplementary Table S3.

B. GO terms analysis for the RNA-seq data. See Supplementary Table S3 for complete list.

C. Fold-change analysis of the 38 genes selected in the initial DepMap screen (Figure 1A and Supplementary Table S1) in FAM53C knock-down cells compared to controls.

1025 **D.** Fold-change analysis for canonical p53 target genes in FAM53C knock-down cells compared
1026 to controls.

1027 **E.** Immunoassay for p21 in control and p53 knock-out RPE-1 cells in control and FAM53C knock-
1028 down cells. HSP90 serves as a loading control (N=1). Values on the bottom represent the ratio
1029 between the signal for p21 and the signal for HSP90 in the same lane.

1030 **F.** Representative example of FACS analysis for BrdU/PI staining of RPE-1 cells in control and
1031 p53 knockout RPE-1 cells as in Figure 2C.

1032 **G.** Representative example of flow cytometry analysis for BrdU/PI staining of RPE-1 cells in
1033 control and RB knockout RPE-1 cells as in Figure 2D.

1034 **H.** Representative example of flow cytometry analysis for BrdU/PI staining of RPE-1 cells in
1035 control and FAM53C-overexpressing RPE-1 cells as in Figure 2E.

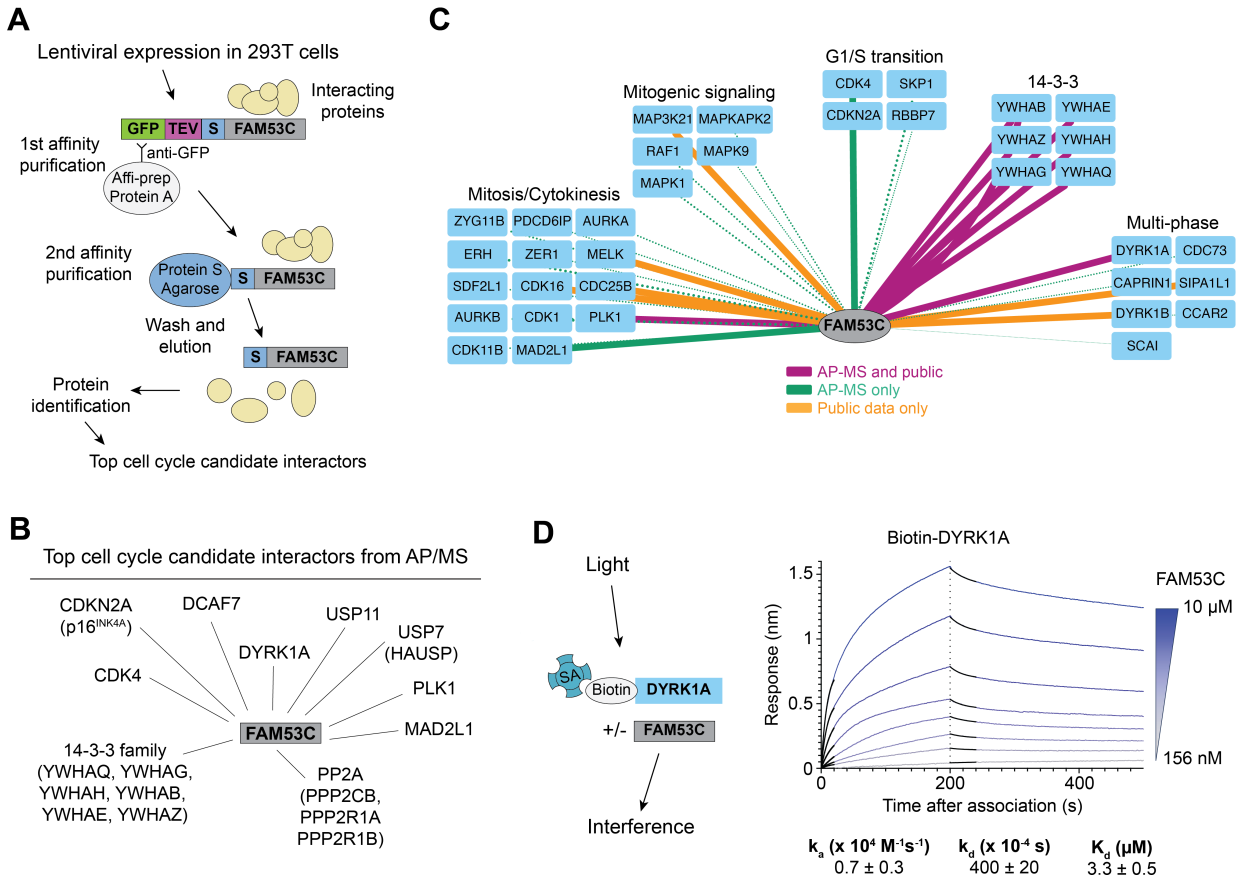

Figure 3: The FAM53C interactome identifies cell cycle factors

A. Cartoon representation of the AP/MS experiment to determine the FAM53C interactome.

B. Top cell cycle interactors from the AP/MS experiment. See Supplementary Tables S4 and S5 for the complete list.

C. CytoTRACE analysis integrating the results of the AP-MS experiment with public databases. Solid lines indicate $p \leq 0.05$, and line thickness correlates to pNSAF from AP-MS experiment.

D. Biolayer interferometry assay to measure the binding of recombinant FAM53C to DYRK1A-coated streptavidin (SA) sensors. Association begins a 0 seconds. Dotted line indicates start of dissociation phase. Black solid line indicates portion of the curve that was analyzed for on and off rates. Reported rate constants are from data fitting of observed on and off rates and the equilibrium constant was determined from the steady-state response analysis.

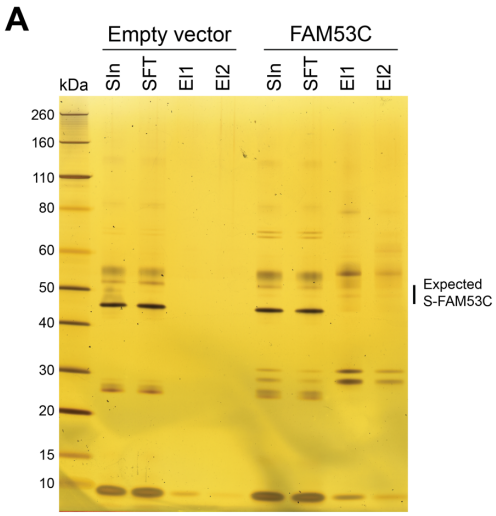

Figure S3, related to Figure 3: The FAM53C interactome identifies cell cycle factors

A. Silver stain of protein fractions in the AP/MS experiment. Sin: S-bead input (cleavage of protein from the GFP-beads before binding to s-beads); SFT: S-bead flowthrough (solution after binding to s-bead). E1, E2: elution 1 and elution 2 from S-beads.

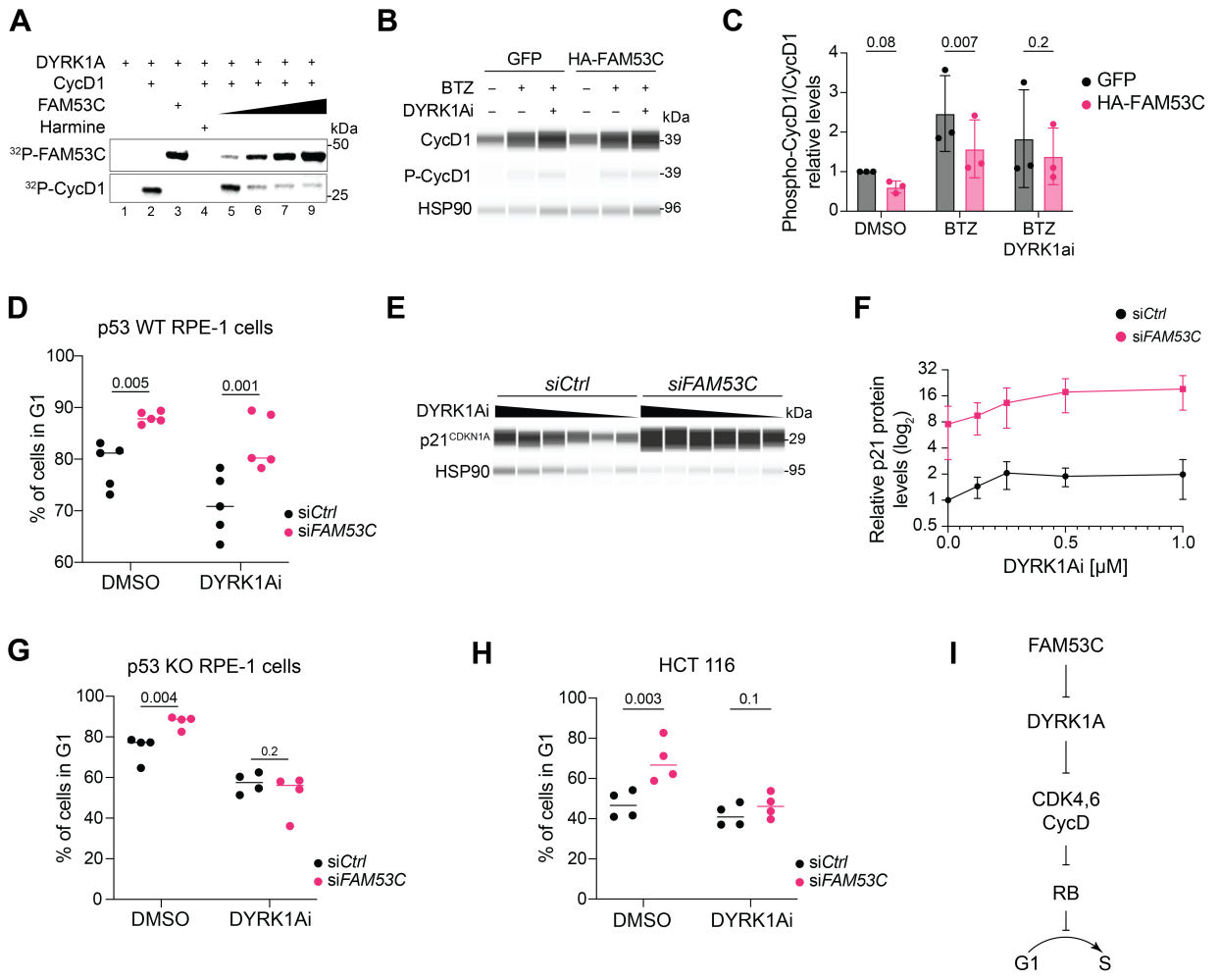

Figure 4: FAM53C controls cell cycle progression in part via DYRK1A

A. *In vitro* phosphorylation assay. Recombinantly expressed Cyclin D1 (1 μM) was phosphorylated by DYRK1A (200 nM) for 15 min alone or in the presence of increasing amounts of FAM53C. FAM53C concentration was 5 mM (lane #3) or 1, 2.5, 5, and 10 mM (lanes #5-8). Lane #1 contains DYRK1A without substrate. The DYRK1A kinase inhibitor Harmine was added at 25 μM. Representative experiment of N=3 experiments.

B. Representative immunoassay for Cyclin D1 and phospho-Cyclin D1 in RPE-1 cells expressing GFP or FAM53C with DMSO or treated with 500 nM bortezomib for two hours, with or without the SM13797 DYRK1A kinase inhibitor (DYRK1Ai). HSP90 serves as a loading control.

C. Quantification of (B).

D. Fraction of cells in G1 from BrdU/PI staining in control (p53 wild-type, WT) RPE-1 cells, with DMSO control or treatment with the SM13797 DYRK1Ai (N=3).

E. Representative immunoassay for p21 protein levels in RPE-1 cells treated with different concentration of the SM13797 DYRK1Ai.

F. Quantification of (E) at different concentrations of the SM13797 DYRL1Ai (N=3 per concentration).

1070 **G.** As in (D) with p53 knockout (KO) RPE-1 cells (N=4).

1071 **H.** As in (D) with HCT116 colon cancer cells (N=4).

1072 **I.** Cartoon placing FAM53C upstream of DYRK1A and the CycD/CDK4,6-RB pathway in G1.

1073 P-values for (C), (D), (G), (H) calculated by paired t-test.

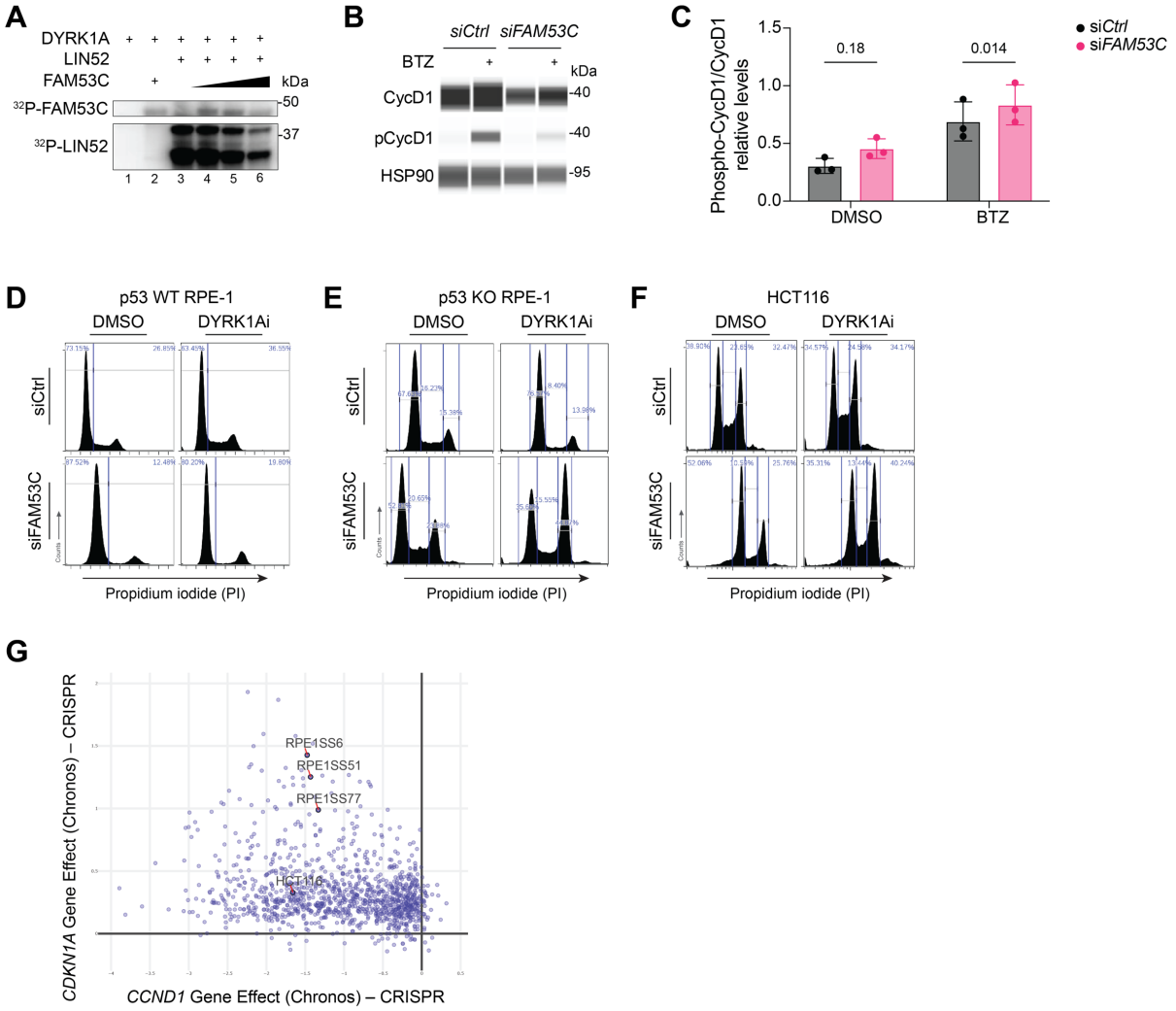

Figure S4, related to Figure 4: FAM53C controls cell cycle progression in part via DYRK1A

A. Recombinantly expressed LIN52 (10 μM) was phosphorylated by DYRK1A (400 nM) for 30 min alone or in the presence of increasing amounts of FAM53C. FAM53C concentration was 1.6, 5, 15 μM (lanes #4-6). Lane #1 contains DYRK1A without substrate. Representative experiment of N=2 experiments.

B. Representative immunoassay for Cyclin D1 and phospho-Cyclin D1 in control and FAM53C knock-down RPE-1 cells. HSP90 serves as a loading control.

C. Quantification of (B).

D. Representative example of flow cytometry analysis for PI staining of p53 WT RPE-1 cells treated with DMSO or the DYRK1Ai, as in Figure 4D.

E. As in (D) for p53 KO RPE-1 cells, as in Figure 4G.

F. As in (D) for HCT116 cells, as in Figure 4H.

G. Correlation for the gene effects of *CCND1* and *CDKN1A* (coding for Cyclin D1 and p21, respectively) the DepMap CRISPR dataset. RPE1SS6, RPE1SS51, and RPE1SS77 are three derivatives of RPE-1 cells.

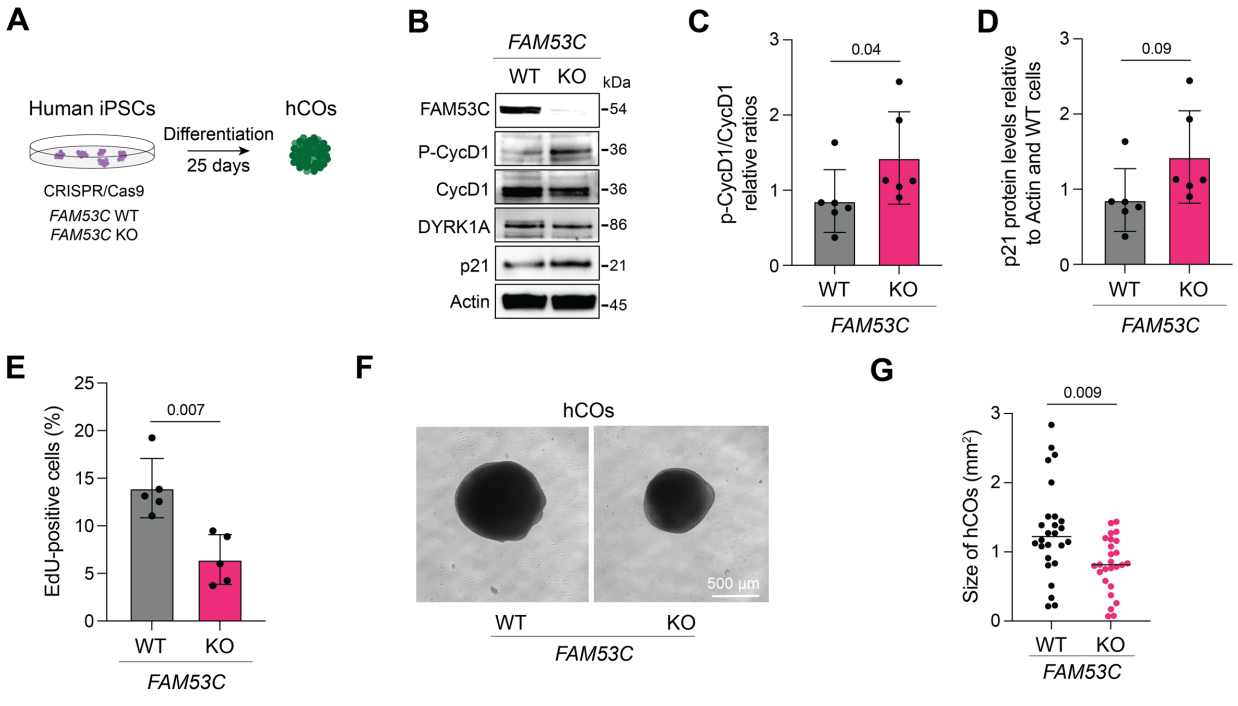

Figure 5: Loss of FAM53C impairs the development of human cortical organoids.

A. Cartoon of the differentiation protocol from human induced pluripotent stem cells (iPSCs) to human cortical organoids (hCOs).

B. Representative immunoblot analysis of wild-type (WT) and *FAM53C* knockout (KO) hCOs. Actin serves as a loading control.

C. Quantification of (B) for phospho-Cyclin D1 relative to Cyclin D1 levels.

D. Quantification of (B) for p21 levels relative to Actin levels.

E. Quantification of Edu-positive cells in wild-type and knockout hCOs.

F. Representative images of wild-type and knockout hCOs. Scale bar, 500 µm.

G. Quantification of (F).

P-values for (C), (D), (E), (G) calculated by paired t-test.

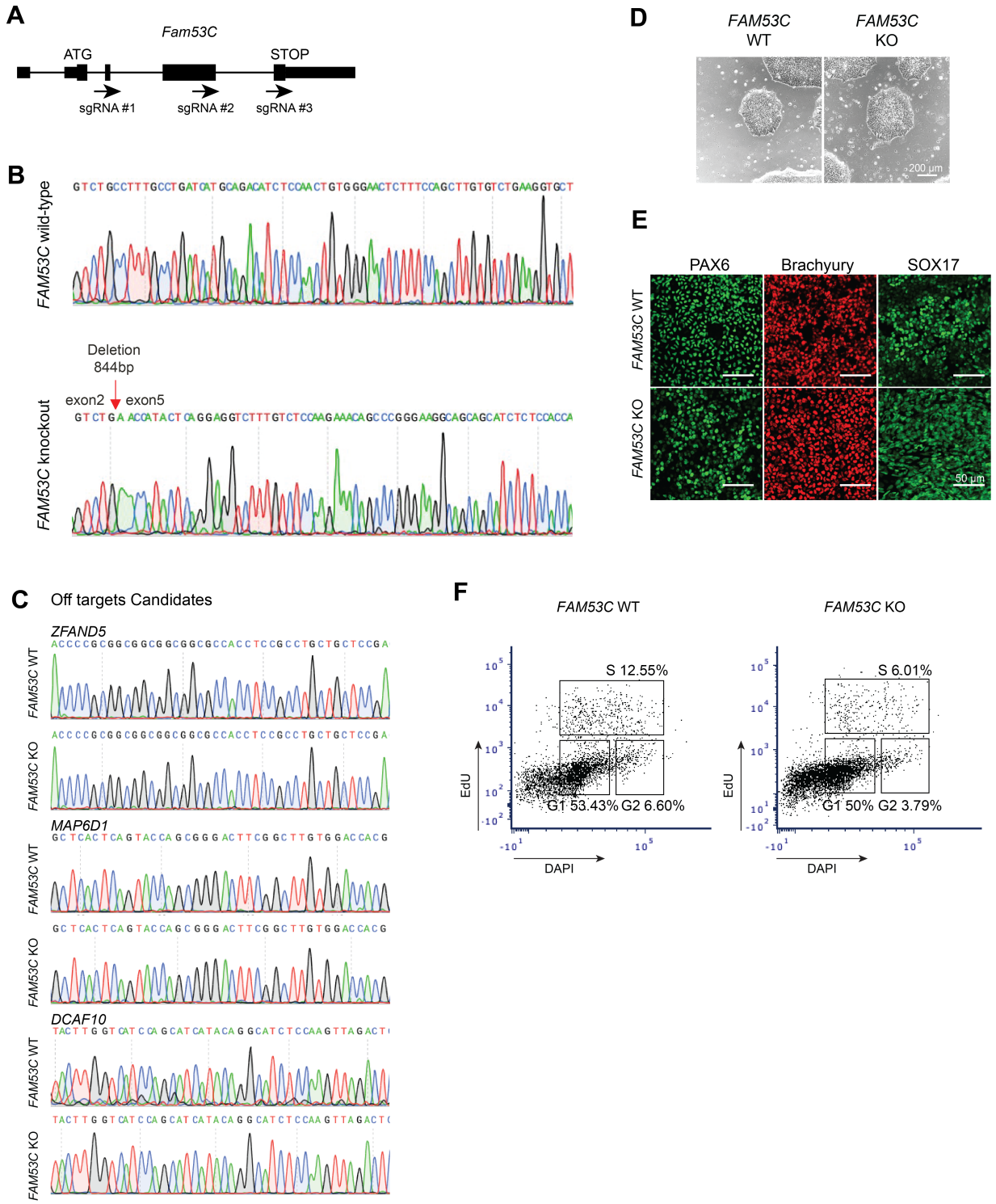

Figure S5, related to Figure 5: Loss of FAM53C impairs the development of human cortical organoids.

A. Cartoon of the *FAM53C* human gene, with the location of the sgRNAs used to knockout the gene in iPSCs (not to scale).

1107 **B.** Sequence histogram showing gene inactivation upon CRISPR/Cas9-mediated deletion.

1108 **C.** Sequence histogram showing no changes in the sequence of possible off target genes.

1109 **D.** Representative images of wild-type and knockout iPSC colonies. Scale bar, 200 μm.

1110 **E.** Representative images of immunofluorescence staining of pluripotency markers in wild-type
1111 and knockout iPSCs. Scale bar, 50 μm.

1112 **F.** Representative example of flow cytometry analysis for EdU/DAPI staining of hCOs, as in Figure
1113 4E.

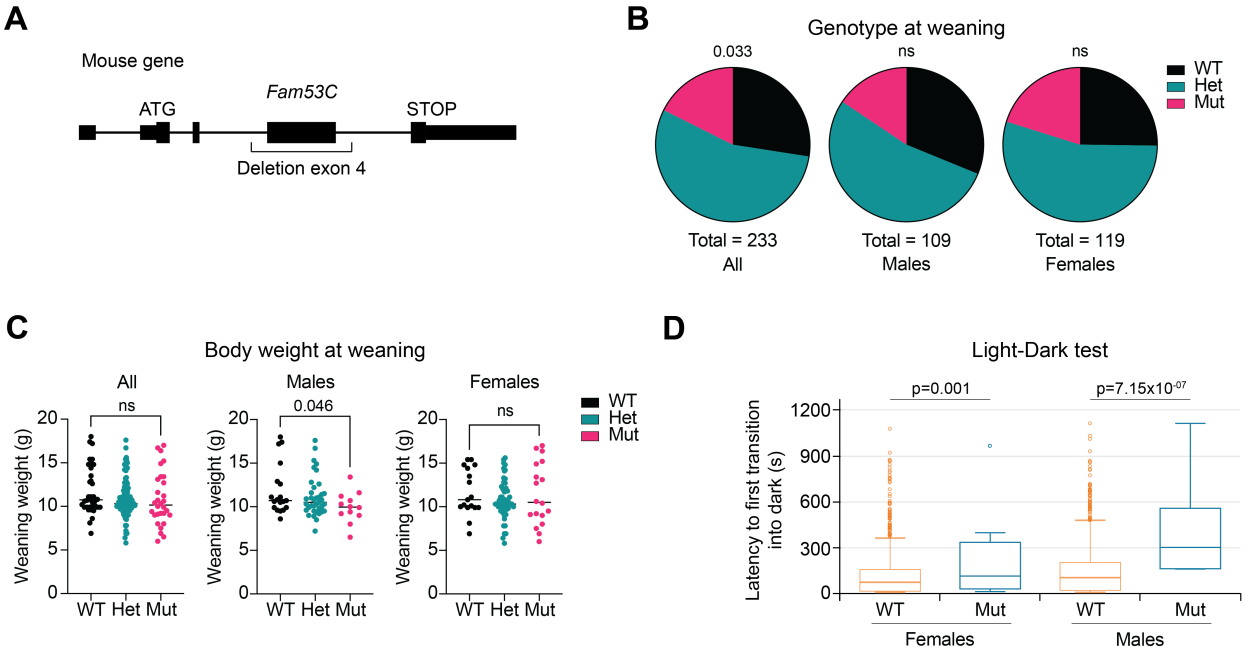

Figure 6

A. Cartoon of the *Fam53C* mutant allele, with deletion of the major coding exon (exon 4) (not to scale).

B. Genotypes of mouse pups at weaning from *Fam53C*$^{+/-}$ crosses at the IMPC facility. WT: wild-type; Het, heterozygous mutant mice; Mut, homozygous mutant mice.

C. Body weight analysis at weaning for mice generated by *Fam53C*$^{+/-}$ crosses.

D. Measure of the latency to first transition into a dark chamber (Light-Dark test) for control (n=1998 males and n=2037 females) and *Fam53C* knockout mice (n=6 males and n=7 females).

P-values for (B) calculated by a Chi-squared test. P-values for (C) calculated by unpaired t tests. The details of the Linear Mixed Model framework for statistical analysis for (D) are available on the IMPC web site.

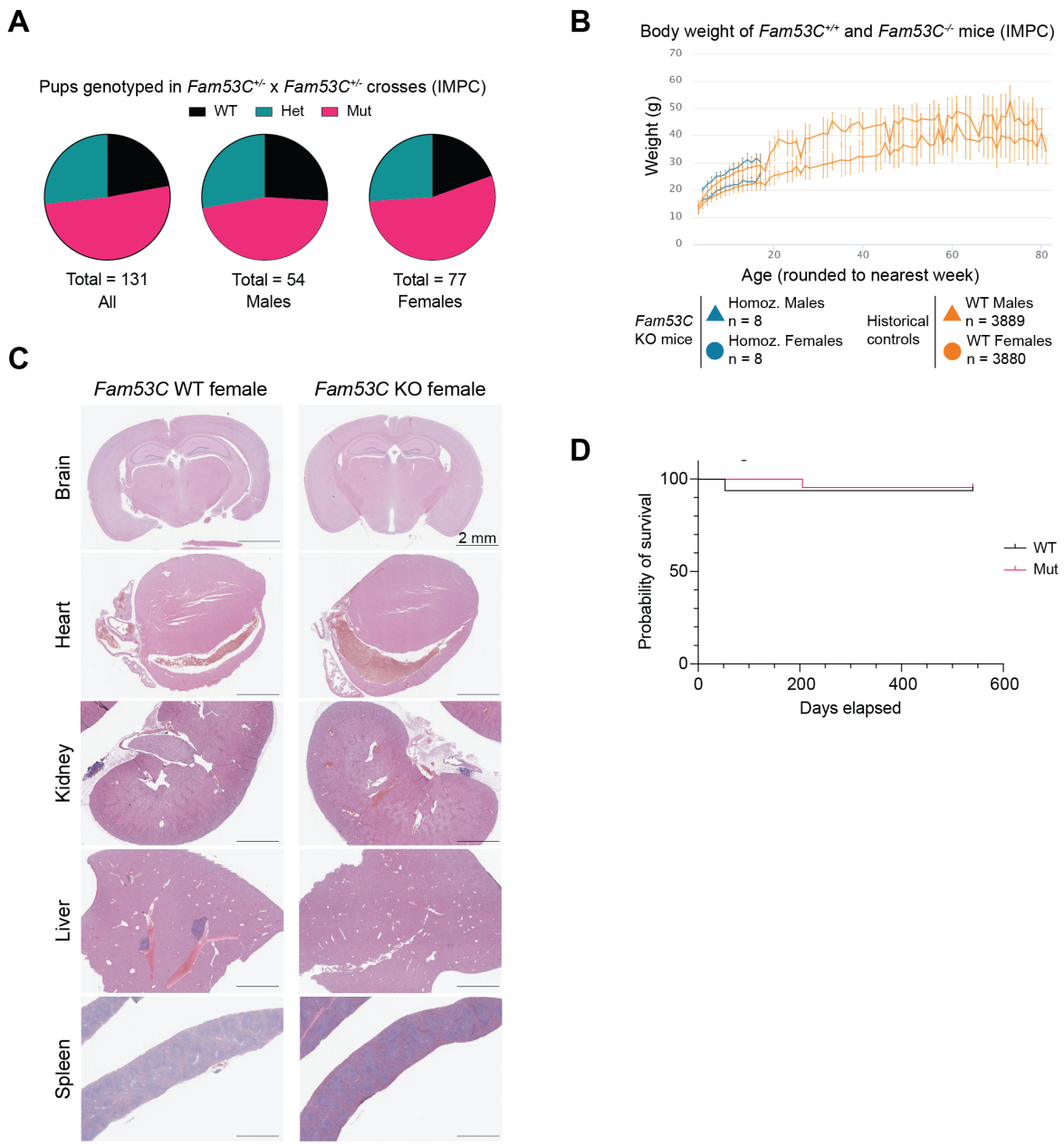

Figure S6, related to Figure 6

A. Genotypes of mouse pups at weaning from *Fam53C*$^{+/-}$ crosses at the IMPC facility.

B. Body weight analysis of a large cohort of historical controls and *Fam53C*$^{-/-}$ mice.

C. Histological analyses (sections stained with hematoxylin and eosin, H&E) for the indicated tissues from mice generated by *Fam53C*$^{+/-}$ crosses. Representative images for one wild-type and one knockout female are shown out of two females and two males analyzed (age, 18 months). Scale bar, 2 mm.

D. Survival analysis for N=23 *Fam53C*$^{-/-}$ mice (7 males and 15 females) and N=16 wild-type controls (7 males and 9 females) from heterozygous crosses. The analysis was stopped at 18 months.

FIGURE 1

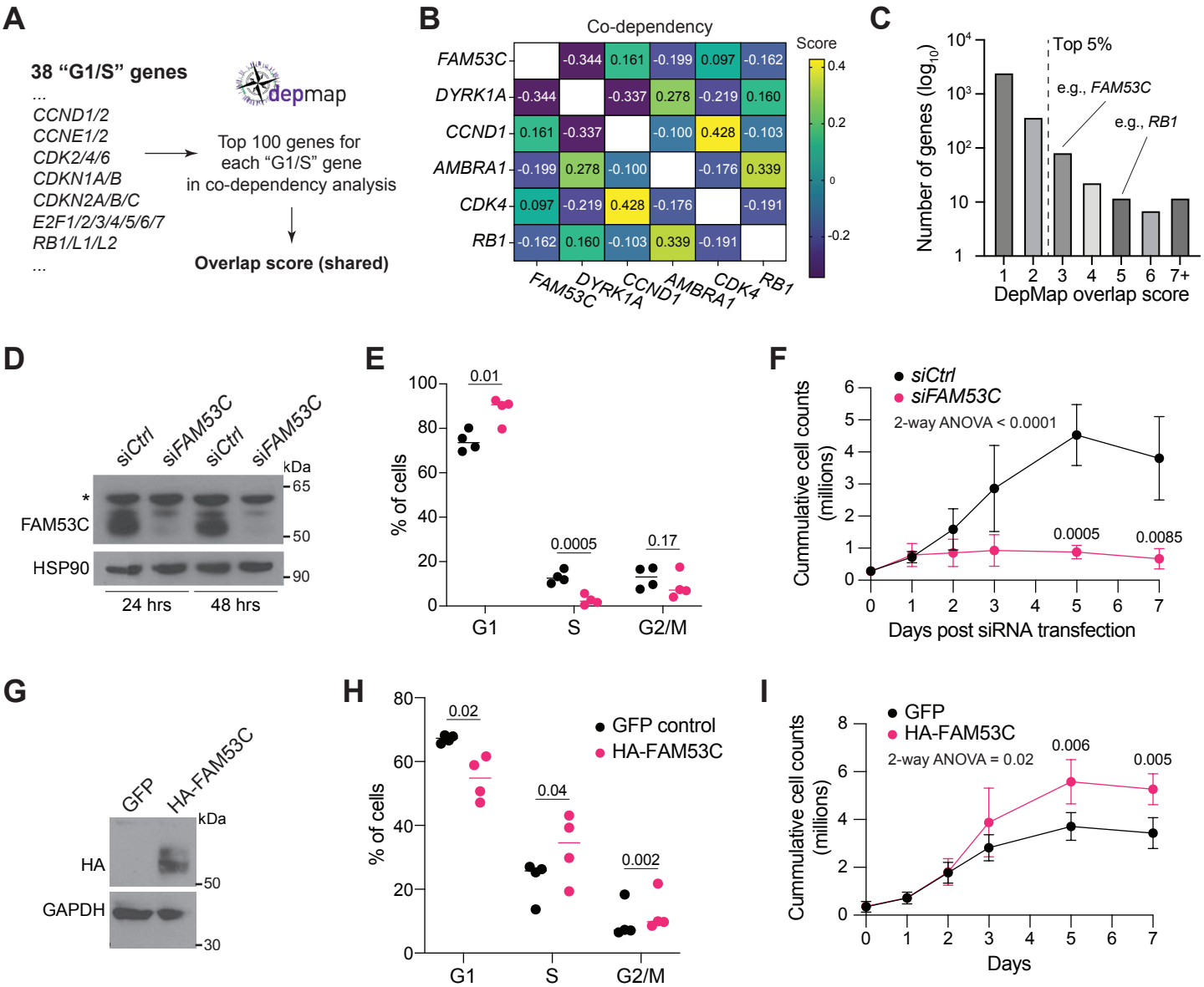
A
38 "G1/S" genes
...
CCND1/2
CCNE1/2
CDK2/4/6
CDKN1A/B
CDKN2A/B/C
E2F1/2/3/4/5/6/7
RB1/L1/L2
...
depmap
Top 100 genes for each "G1/S" gene in co-dependency analysis
Overlap score (shared)
B
Co-dependency
Score
FAM53C
DYRK1A
CCND1
AMBRA1
CDK4
RB1
C
Top 5%
e.g., FAM53C
e.g., RB1
Number of genes (log10)
DepMap overlap score
D
siCtrl
siFAM53C
kDa
FAM53C
HSP90
24 hrs
48 hrs
E
% of cells
G1
S
G2/M
F
siCtrl
siFAM53C
2-way ANOVA < 0.0001
Cummulative cell counts (millions)
Days post siRNA transfection
G
GFP
HA-FAM53C
HA
GAPDH
H
GFP control
HA-FAM53C
I
GFP
HA-FAM53C
2-way ANOVA = 0.02
Days

FIGURE 2

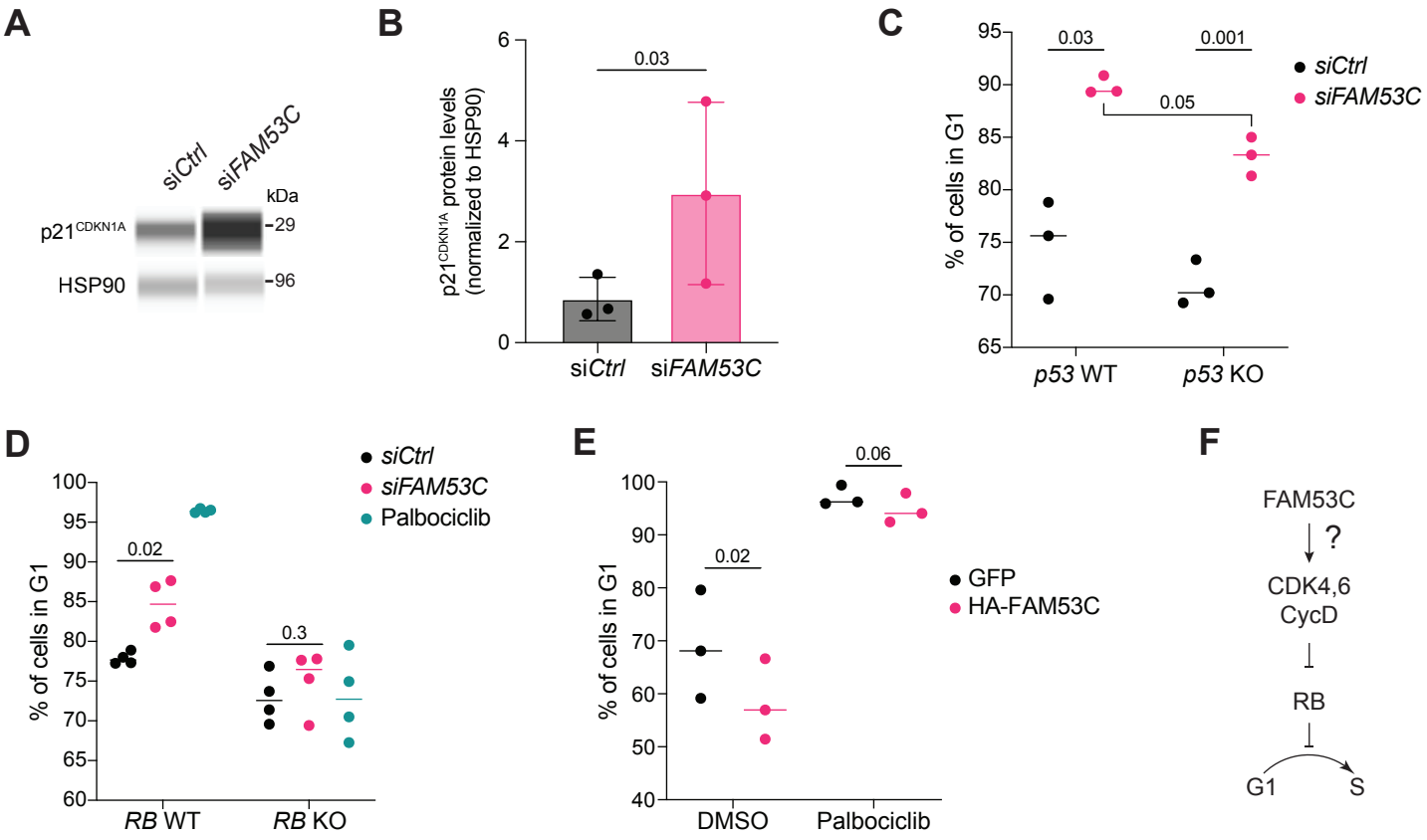
A
siCtrl
siFAM53C
kDa
p21CDKN1A
-29
HSP90
-96
B
p21CDKN1A protein levels (normalized to HSP90)
0.03
siCtrl
siFAM53C
C
% of cells in G1
0.03
0.001
0.05
siCtrl
siFAM53C
p53 WT
p53 KO
D
% of cells in G1
siCtrl
siFAM53C
Palbociclib
0.02
0.3
RB WT
RB KO
E
% of cells in G1
0.06
0.02
GFP
HA-FAM53C
DMSO
Palbociclib
F
FAM53C
?
CDK4,6
CycD
RB
G1
S

FIGURE 3

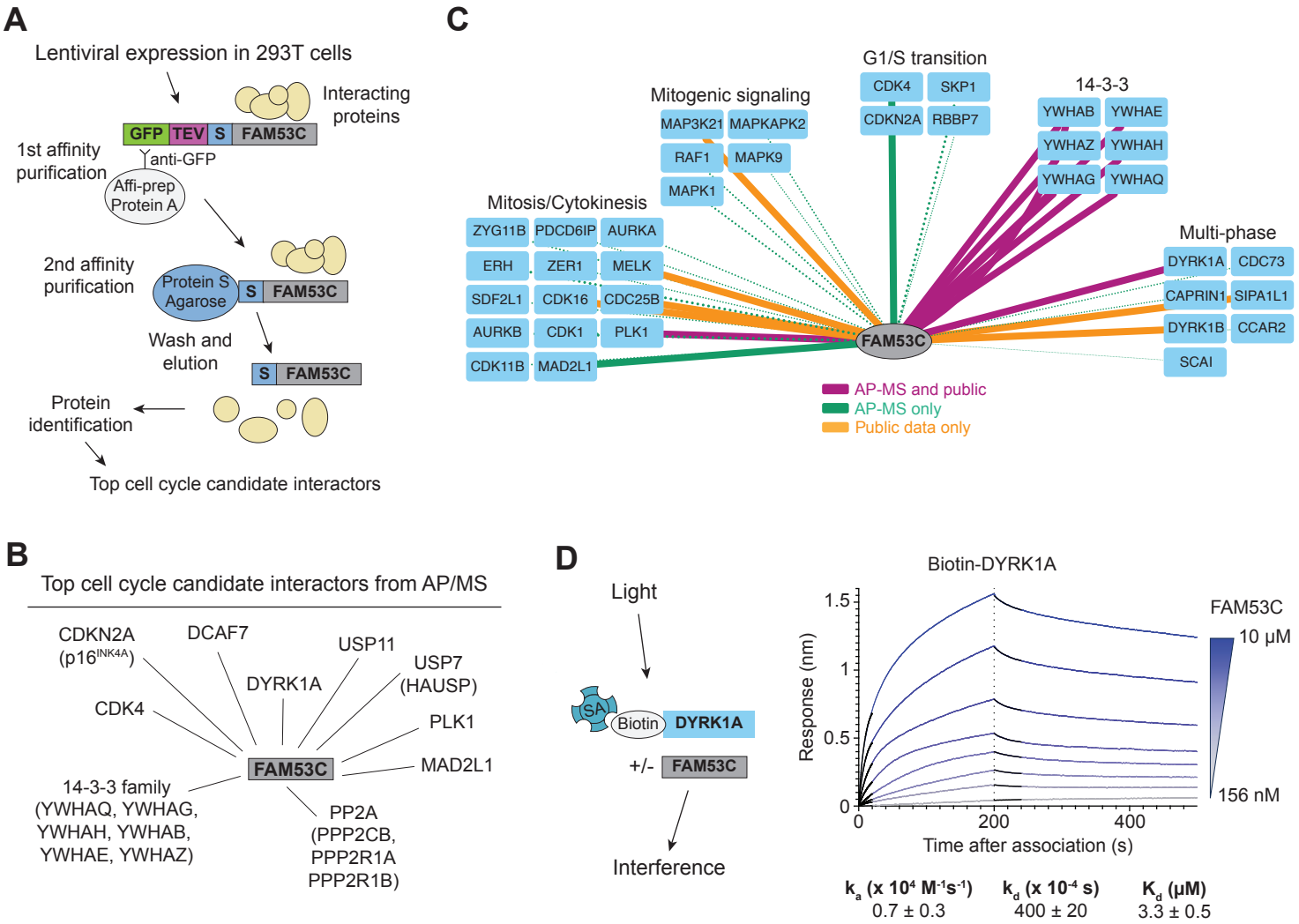
A
Lentiviral expression in 293T cells
Interacting proteins
GFP
TEV
S
FAM53C
1st affinity purification
anti-GFP
Affi-prep Protein A
2nd affinity purification
Protein S Agarose
S
FAM53C
Wash and elution
S
FAM53C
Protein identification
Top cell cycle candidate interactors
C
G1/S transition
CDK4
SKP1
CDKN2A
RBBP7
14-3-3
YWHAB
YWHAE
YWHAZ
YWHAH
YWHAG
YWHAQ
Mitogenic signaling
MAP3K21
MAPKAPK2
RAF1
MAPK9
MAPK1
Mitosis/Cytokinesis
ZYG11B
PDCD6IP
AURKA
ERH
ZER1
MELK
SDF2L1
CDK16
CDC25B
AURKB
CDK1
PLK1
CDK11B
MAD2L1
FAM53C
Multi-phase
DYRK1A
CDC73
CAPRIN1
SIPA1L1
DYRK1B
CCAR2
SCAI
AP-MS and public
AP-MS only
Public data only
B
Top cell cycle candidate interactors from AP/MS
CDKN2A (p16INK4A)
DCAF7
USP11
USP7 (HAUSP)
DYRK1A
CDK4
PLK1
FAM53C
MAD2L1
14-3-3 family (YWHAQ, YWHAG, YWHAH, YWHAB, YWHAE, YWHAZ)
PP2A (PPP2CB, PPP2R1A PPP2R1B)
D
Light
SA
Biotin
DYRK1A
+/-
FAM53C
Interference
Biotin-DYRK1A
FAM53C
10 μM
156 nM
Response (nm)
1.5
1
0.5
0
0
200
400
Time after association (s)
ka (x 10⁴ M⁻¹s⁻¹)
0.7 ± 0.3
kd (x 10⁻⁴ s)
400 ± 20
Kd (μM)
3.3 ± 0.5

FIGURE 4

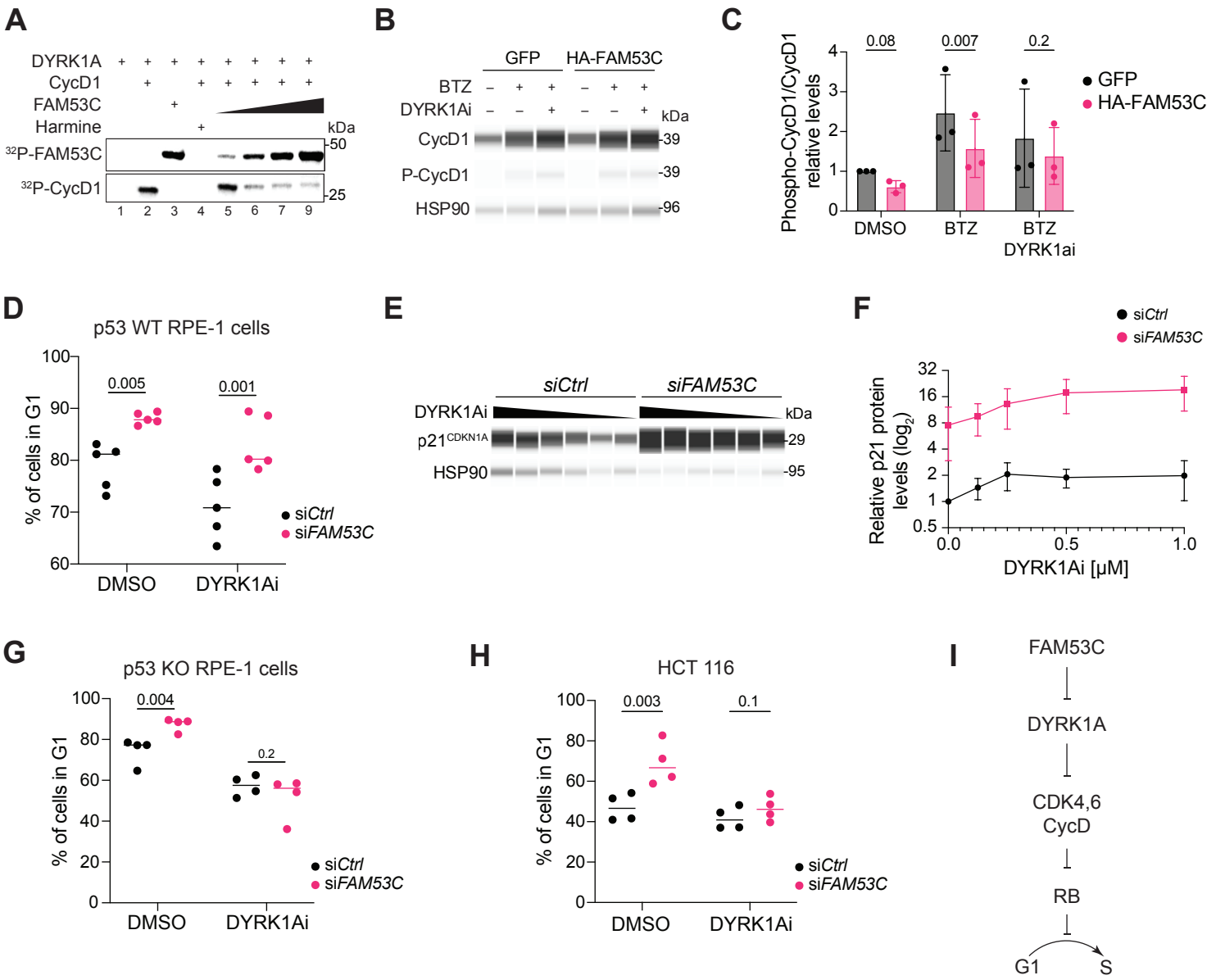
A
DYRK1A
CycD1
FAM53C
Harmine
kDa
32P-FAM53C
32P-CycD1
50
25
1 2 3 4 5 6 7 9
B
GFP
HA-FAM53C
BTZ
DYRK1Ai
kDa
CycD1
P-CycD1
HSP90
39
39
96
C
Phospho-CycD1/CycD1 relative levels
0.08
0.007
0.2
GFP
HA-FAM53C
DMSO
BTZ
BTZ DYRK1ai
D
p53 WT RPE-1 cells
% of cells in G1
0.005
0.001
siCtrl
siFAM53C
DMSO
DYRK1Ai
E
siCtrl
siFAM53C
DYRK1Ai
kDa
p21CDKN1A
HSP90
29
95
F
siCtrl
siFAM53C
Relative p21 protein levels (log2)
DYRK1Ai [μM]
G
p53 KO RPE-1 cells
% of cells in G1
0.004
0.2
siCtrl
siFAM53C
DMSO
DYRK1Ai
H
HCT 116
% of cells in G1
0.003
0.1
siCtrl
siFAM53C
DMSO
DYRK1Ai
I
FAM53C
DYRK1A
CDK4,6
CycD
RB
G1
S

FIGURE 5

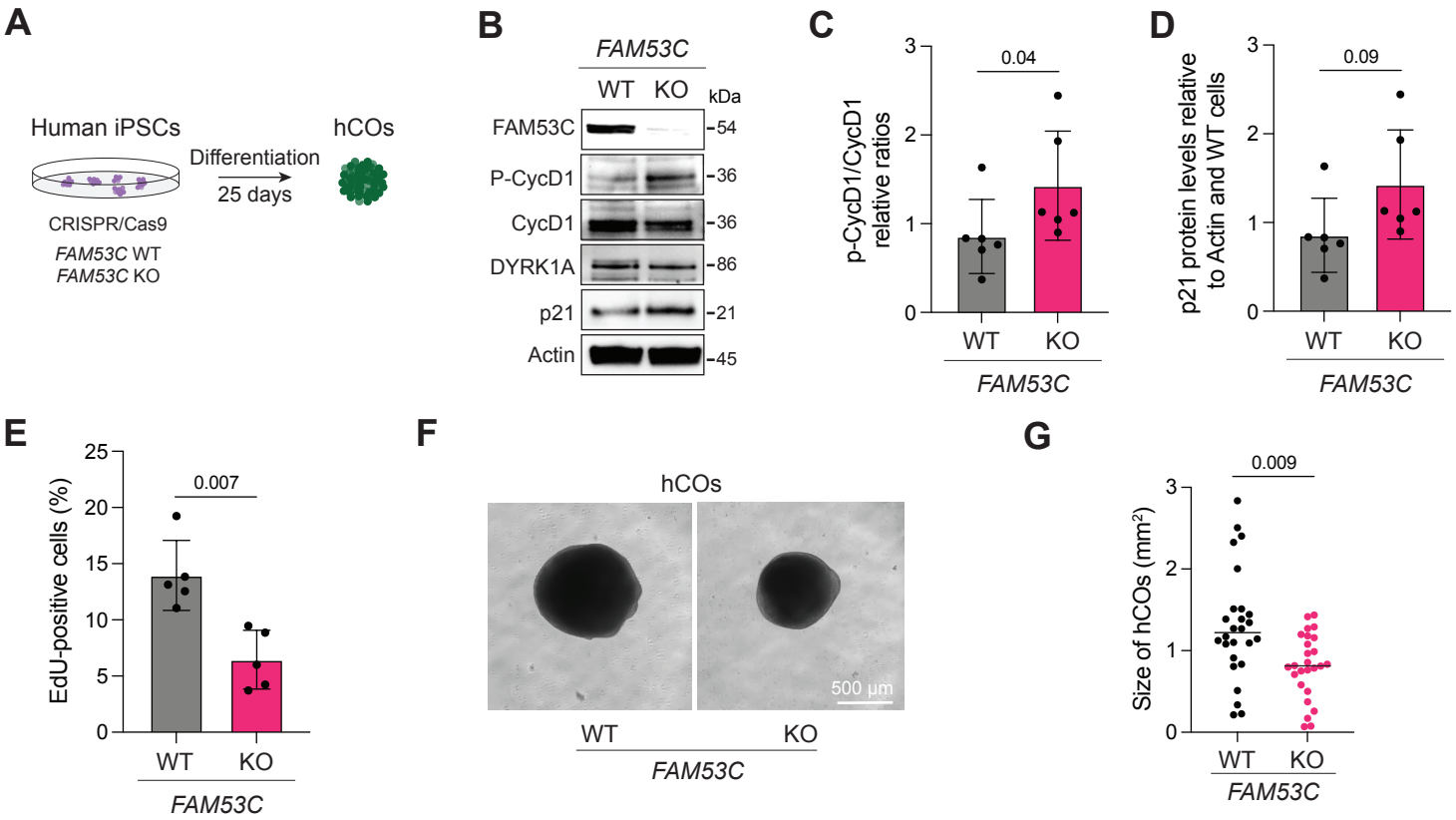
A
Human iPSCs
Differentiation
25 days
hCOs
CRISPR/Cas9
FAM53C WT
FAM53C KO
B
FAM53C
WT KO
kDa
FAM53C
P-CycD1
CycD1
DYRK1A
p21
Actin
54
36
36
86
21
45
C
p-CycD1/CycD1 relative ratios
0.04
WT KO
FAM53C
D
p21 protein levels relative to Actin and WT cells
0.09
WT KO
FAM53C
E
EdU-positive cells (%)
0.007
WT KO
FAM53C
F
hCOs
500 µm
WT KO
FAM53C
G
Size of hCOs (mm²)
0.009
WT KO
FAM53C

FIGURE 6

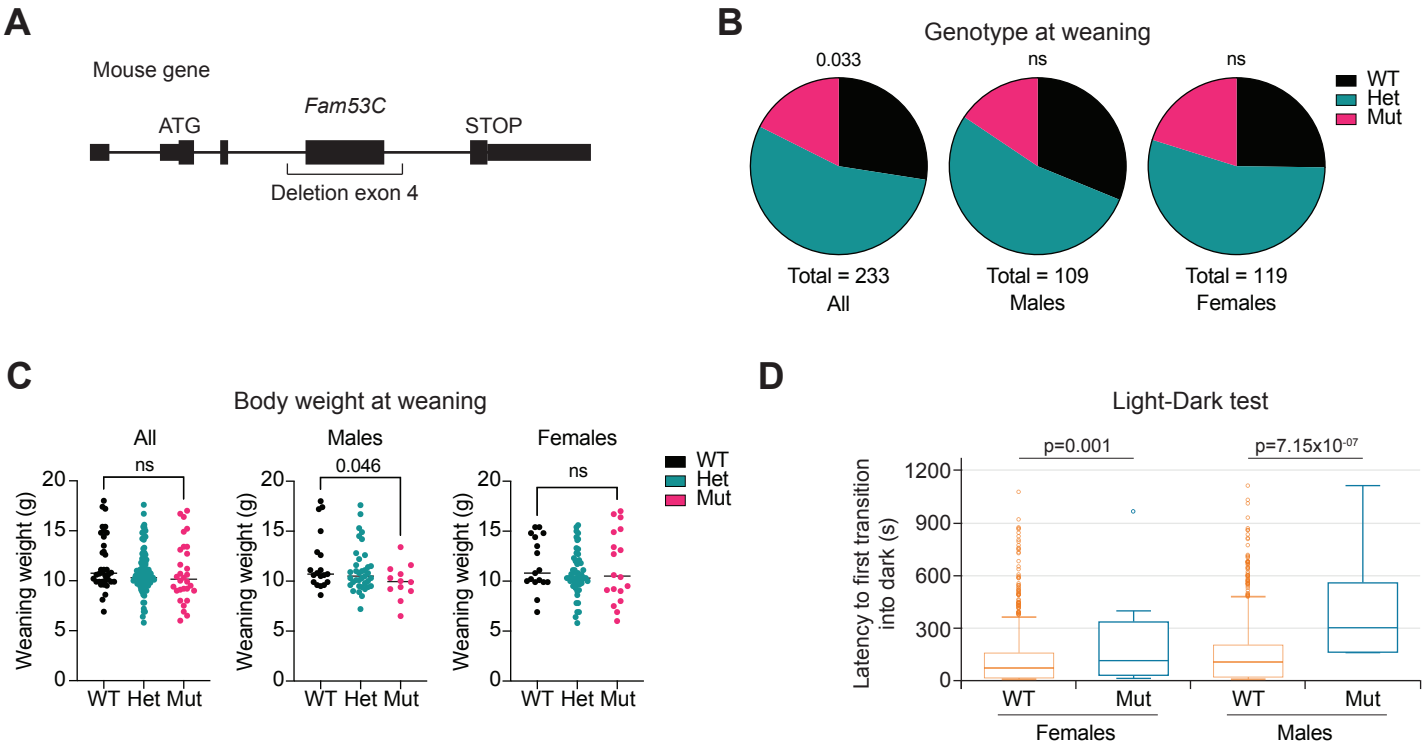
A
Mouse gene
ATG
Fam53C
STOP
Deletion exon 4
B
Genotype at weaning
0.033
ns
ns
WT
Het
Mut
Total = 233
All
Total = 109
Males
Total = 119
Females
C
Body weight at weaning
All
Males
Females
ns
0.046
ns
Weaning weight (g)
WT Het Mut
D
Light-Dark test
p=0.001
p=7.15x10-07
Latency to first transition into dark (s)
WT
Mut
Females
Males

FIGURE S1

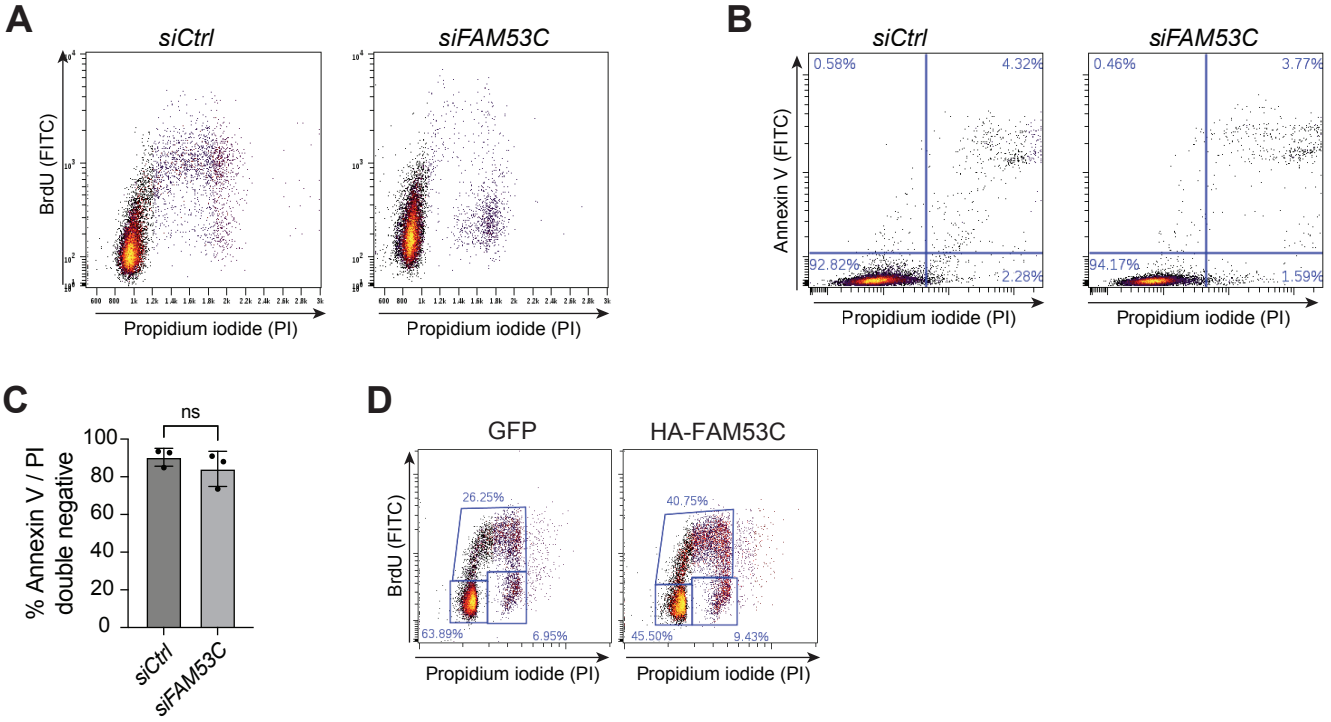
A
siCtrl
siFAM53C
BrdU (FITC)
Propidium iodide (PI)
B
siCtrl
siFAM53C
Annexin V (FITC)
0.58%
4.32%
92.82%
2.28%
0.46%
3.77%
94.17%
1.59%
Propidium iodide (PI)
C
ns
% Annexin V / PI double negative
100
80
60
40
20
0
siCtrl
siFAM53C
D
GFP
HA-FAM53C
BrdU (FITC)
26.25%
63.89%
6.95%
40.75%
45.50%
9.43%
Propidium iodide (PI)

FIGURE S2

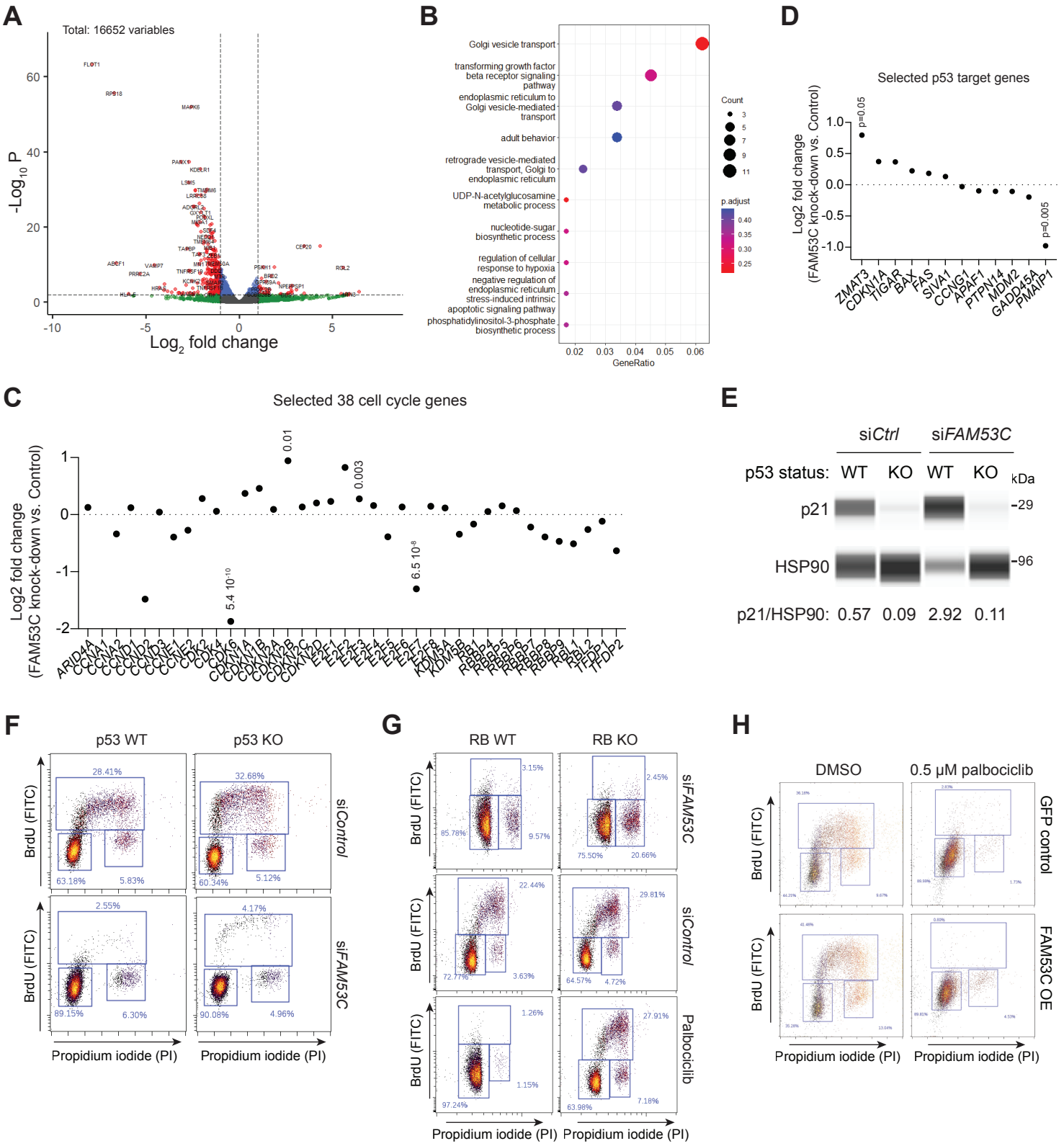
A
Total: 16652 variables
-Log10 P
Log2 fold change
B
Golgi vesicle transport
transforming growth factor beta receptor signaling pathway
endoplasmic reticulum to Golgi vesicle-mediated transport
adult behavior
retrograde vesicle-mediated transport, Golgi to endoplasmic reticulum
UDP-N-acetylglucosamine metabolic process
nucleotide-sugar biosynthetic process
regulation of cellular response to hypoxia
negative regulation of endoplasmic reticulum stress-induced intrinsic apoptotic signaling pathway
phosphatidylinositol-3-phosphate biosynthetic process
Count
p.adjust
GeneRatio
D
Selected p53 target genes
Log2 fold change (FAM53C knock-down vs. Control)
p=0.05
p=0.005
ZMAT3
CDKN1A
TIGAR
BAX
FAS
SIVA1
CCNG1
APAF1
PTPN14
MDM2
GADD45A
PMAIP1
C
Selected 38 cell cycle genes
Log2 fold change (FAM53C knock-down vs. Control)
0.01
0.003
5.4 10-10
6.5 10-8
E
siCtrl
siFAM53C
p53 status: WT KO WT KO
kDa
p21
HSP90
29
96
p21/HSP90: 0.57 0.09 2.92 0.11
F
p53 WT
p53 KO
BrdU (FITC)
Propidium iodide (PI)
siControl
siFAM53C
28.41%
63.18%
5.83%
32.68%
60.34%
5.12%
2.55%
89.15%
6.30%
4.17%
90.08%
4.96%
G
RB WT
RB KO
BrdU (FITC)
Propidium iodide (PI)
siFAM53C
siControl
Palbociclib
3.15%
85.78%
9.57%
2.45%
75.50%
20.66%
22.44%
72.77%
3.63%
29.81%
64.57%
4.72%
1.26%
97.24%
1.15%
27.91%
63.98%
7.18%
H
DMSO
0.5 μM palbociclib
BrdU (FITC)
Propidium iodide (PI)
GFP control
FAM53C OE

FIGURE S3

A

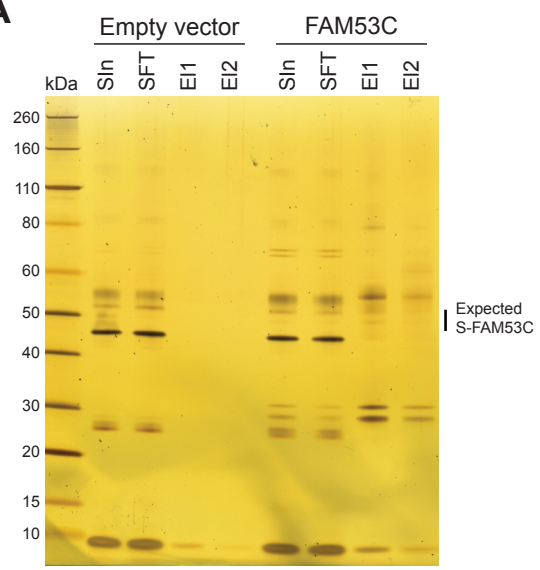
Empty vector
FAM53C
kDa
SIn
SFT
EI1
EI2
SIn
SFT
EI1
EI2
260
160
110
80
60
50
40
30
20
15
10
Expected
S-FAM53C

FIGURE S4

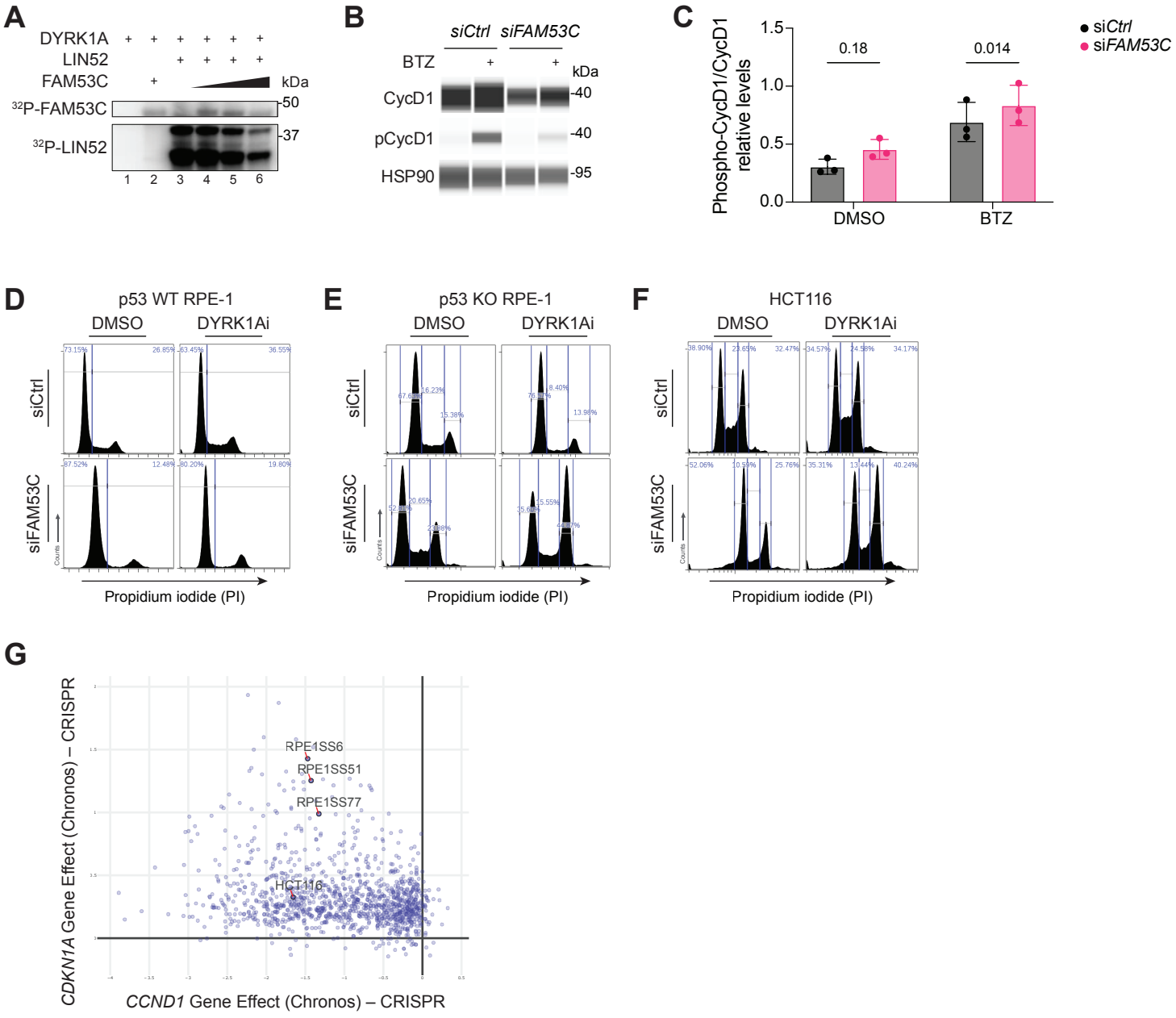
A
DYRK1A
LIN52
FAM53C
kDa
32P-FAM53C
32P-LIN52
50
37
1 2 3 4 5 6
B
siCtrl siFAM53C
BTZ
kDa
CycD1
pCycD1
HSP90
40
40
95
C
Phospho-CycD1/CycD1 relative levels
1.5
1.0
0.5
0.0
0.18
0.014
DMSO
BTZ
siCtrl
siFAM53C
D
p53 WT RPE-1
DMSO
DYRK1Ai
siCtrl
siFAM53C
Propidium iodide (PI)
E
p53 KO RPE-1
DMSO
DYRK1Ai
siCtrl
siFAM53C
Propidium iodide (PI)
F
HCT116
DMSO
DYRK1Ai
siCtrl
siFAM53C
Propidium iodide (PI)
G
CDKN1A Gene Effect (Chronos) – CRISPR
CCND1 Gene Effect (Chronos) – CRISPR
RPE1SS6
RPE1SS51
RPE1SS77
HCT116

FIGURE S5

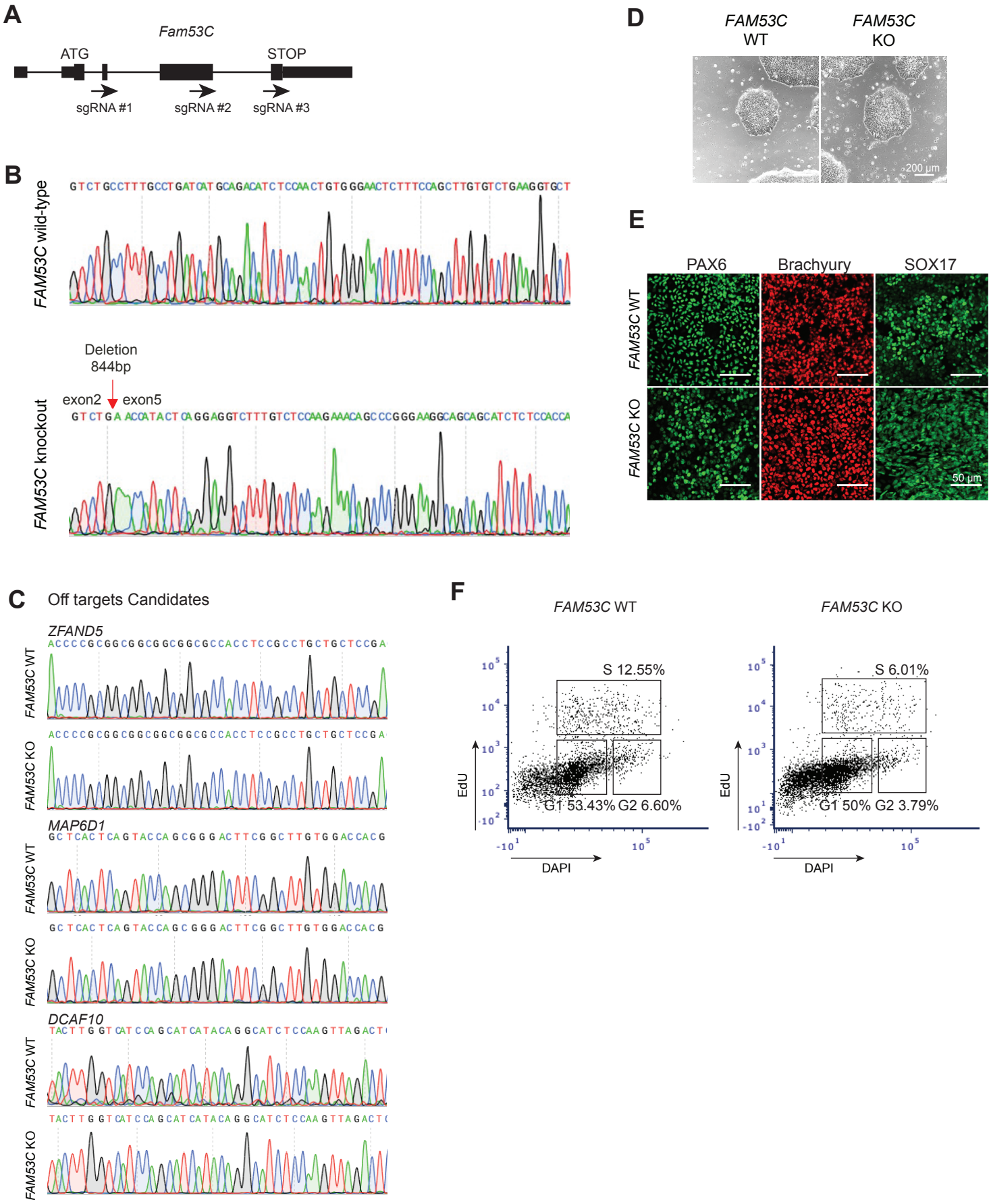
A
Fam53C
ATG
STOP
sgRNA #1
sgRNA #2
sgRNA #3
B
FAM53C wild-type
Deletion
844bp
exon2
exon5
FAM53C knockout
C
Off targets Candidates
ZFAND5
MAP6D1
DCAF10
FAM53C WT
FAM53C KO
D
FAM53C WT
FAM53C KO
200 µm
E
PAX6
Brachyury
SOX17
FAM53C WT
FAM53C KO
50 µm
F
FAM53C WT
FAM53C KO
S 12.55%
G1 53.43%
G2 6.60%
S 6.01%
G1 50%
G2 3.79%
EdU
DAPI

FIGURE S6

A

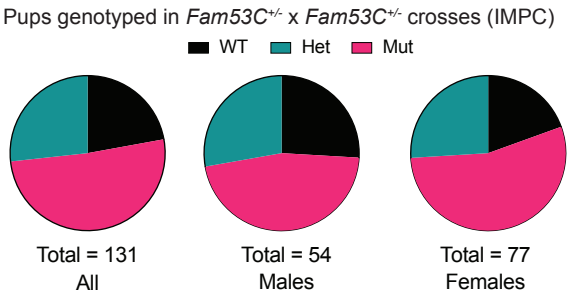

B

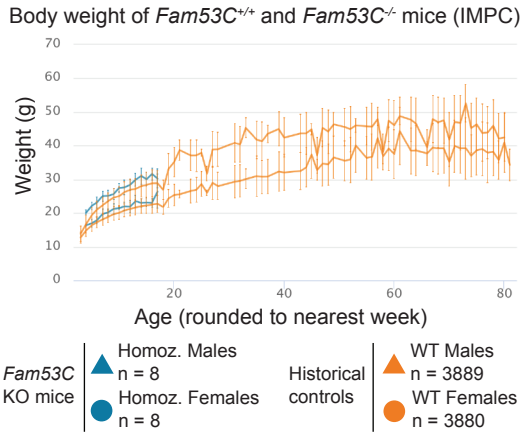

C

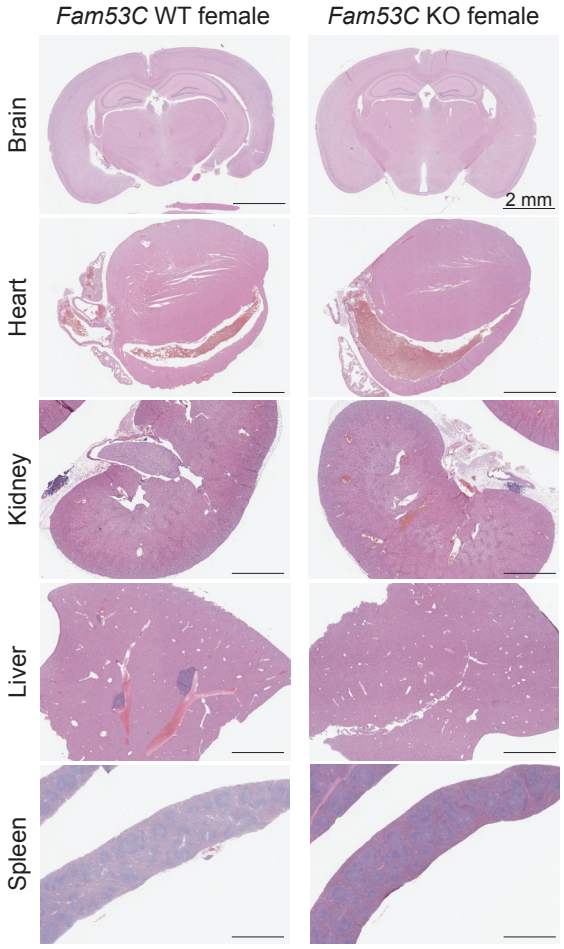
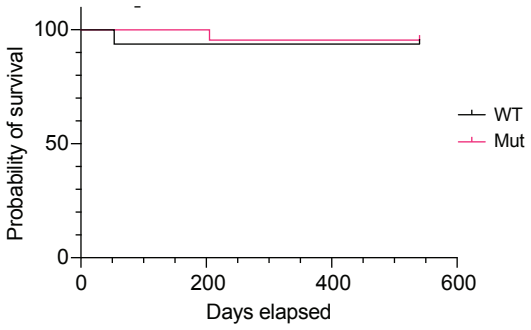
D